HAL open science

ISOW Spreading and Mixing as Revealed by Deep-Argo Floats Launched in the Charlie-Gibbs Fracture Zone

Virginie Racapé, Virginie Thierry, Herlé Mercier, Cécile Cabanes

To cite this version:

Virginie Racapé, Virginie Thierry, Herlé Mercier, Cécile Cabanes. ISOW Spreading and Mixing as Revealed by Deep-Argo Floats Launched in the Charlie-Gibbs Fracture Zone. Journal of Geophysical Research. Oceans, 2019, 10.1029/2019JC015040 . hal-02382468

HAL Id: hal-02382468

https://hal.science/hal-02382468

Submitted on 10 Nov 2021

HAL is a multi-disciplinary open access archive for the deposit and dissemination of scientific research documents, whether they are published or not. The documents may come from teaching and research institutions in France or abroad, or from public or private research centers.

L'archive ouverte pluridisciplinaire **HAL**, est destinée au dépôt et à la diffusion de documents scientifiques de niveau recherche, publiés ou non, émanant des établissements d'enseignement et de recherche français ou étrangers, des laboratoires publics ou privés.

Copyright

Check for updates

AGU100 ADVANCING EARTH AND SPACE SCIENCE

JGR Oceans

RESEARCH ARTICLE
10.1029/2019JC015040

Key Points:
- A direct route is suggested for ISOW from the Charlie-Gibbs Fracture Zone to the Deep Western Boundary Current at Flemish Cap
- At the Charlie-Gibbs Fracture Zone, oxygen measurements are key to quantifying ISOW mixing with North East Atlantic Deep Water
- Mixing between ISOW, North East Atlantic Deep Water, Labrador Sea Water, and Denmark Strait Overflow Water is observed in the western basin

Supporting Information:
- Supporting Information S1

Correspondence to:
V. Racapé and V. Thierry,
virginie.racape@ifremer.fr;
virginie.thierry@ifremer.fr

Citation:
Racapé, V., Thierry, V., Mercier, H., & Cabanes, C. (2019). ISOW spreading and mixing as revealed by Deep-Argo floats launched in the Charlie-Gibbs Fracture Zone. *Journal of Geophysical Research: Oceans*, *124*, 6787–6808. https://doi.org/10.1029/2019JC015040

Received 12 FEB 2019
Accepted 28 AUG 2019
Accepted article online 2 SEP 2019
Published online 14 OCT 2019

©2019. American Geophysical Union. All Rights Reserved.

ISOW Spreading and Mixing as Revealed by Deep-Argo Floats Launched in the Charlie-Gibbs Fracture Zone

Virginie Racapé[1,2], Virginie Thierry[1], Herlé Mercier[3], and Cécile Cabanes[3,2]

[1]Ifremer, University of Brest, CNRS, IRD, Laboratoire d'Océanographie Physique et Spatiale (LOPS), IUEM, Brest, France, [2]University of Brest, CNRS, IRD, Unité Mixte de Service 3113, IUEM, Brest, France, [3]University of Brest, CNRS, Ifremer, IRD, Laboratoire d'Océanographie Physique et Spatiale (LOPS), IUEM, 29280 Brest, France

Abstract To improve our understanding of deep circulation, we deployed five Deep-Argo floats (0–4,000 m) in the Charlie-Gibbs Fracture Zone (CGFZ), which channels the flow of Iceland-Scotland Overflow Water (ISOW), a dense water mass of the North Atlantic Ocean. The floats were programed to drift at 2,750 dbar in the ISOW layer. The floats mainly moved westward in the CGFZ, although some of them followed different routes for few cycles depending on northward intrusions of the North Atlantic Current over the CGFZ. One float revealed a direct route for ISOW from CGFZ to the Deep Western Boundary Current at Flemish Cap. In the CGFZ, oxygen data acquired by the floats revealed that the ISOW layer, characterized by salinity higher than 34.94 and density greater than 27.8 kg/ m, was mainly composed of the highly oxygenated ISOW and the less oxygenated North East Atlantic Deep Water (NEADW), a complex water mass from the East Atlantic. In the ISOW layer, the relative contribution of ISOW was generally larger in the northern valley than in the southern valley of CGFZ. Northward intrusions of the North Atlantic Current above the CGFZ increased the relative contribution of NEADW in the northern valley and favors mixing between ISOW and NEADW. The ISOW-NEADW signal flowing westward from the CGFZ toward the Deep Western Boundary Current was progressively diluted by Labrador Sea Water and Denmark Strait Overflow Water. Oxygen measurements from Deep-Argo floats are essential for a better understanding and characterization of the mixing and spreading of deep water masses.

Plain Language Summary The North Atlantic Ocean contributes to the uptake in the deep ocean of the excess of heat received by Earth due to human activities. The heat redistribution toward the rest of the ocean depends on the deep circulation, which is still largely unknown. To improve our understanding of this deep circulation, we deployed in 2015 and 2017 five Deep-Argo floats in the Charlie-Gibbs Fracture Zone (CGFZ), a gap in the Mid-Atlantic Ridge that constraints the pathway of deep water masses. Those autonomous platforms freely drifted at 2,750 dbar in the core of the Iceland-Scotland Overflow Water (ISOW), a young water mass, rich in O_2, originating from the Nordic Seas. One float revealed a new direct route of ISOW toward the subtropical gyre. The pathway followed by the floats west of the CGFZ depended on northward intrusions of the North Atlantic Current over the CGFZ. This interaction between the North Atlantic Current and the deep flow in the CGFZ favors the mixing of ISOW with the North East Atlantic Deep Water, an old water mass characterized by low O_2. These results advocate for equipping Deep-Argo floats with oxygen sensors to improve understanding of deep circulation and water mass mixing.

1. Introduction

The Irminger, Labrador, and Nordic Seas are regions of dense water mass formation by winter heat loss. These water masses feed the cold limb of the Meridional Overturning Circulation and their redistribution within the rest of the ocean moderates global warming by transferring heat and anthropogenic carbon from the atmosphere to the ocean interior. In recent decades, considerable changes were recorded in both North Atlantic Deep Water and Antarctic Bottom Water (Purkey & Johnson, 2013; Smeed et al., 2014), two water masses that belong to the deep Meridional Overturning Circulation. The sampling of the deep ocean obtained by full-depth hydrographic sections or moorings is nevertheless too sparse in space and time to precisely monitor and understand the spreading and mixing of these deep water masses and their variability (Johnson et al., 2015). As demonstrated by Johnson et al. (2015), Deep-Argo floats would be beneficial to complement repeat hydrographic sections. Both can provide robust estimates of long term changes in heat

content, in anthropogenic carbon as well as in ventilation of the deep ocean interior and thus a better understanding of the fate and impact of climate signals.

In the North Atlantic Ocean, most of the overturning occurs east of Greenland (Lozier et al., 2019). There, the formation of Iceland-Scotland Overflow Water (ISOW), one of the major components of the North Atlantic Deep Water, strongly contributes to this overturning. Indeed, it is formed downstream of the Faroe-Shetland channel (Hansen & Østerhus, 2007) and the Iceland-Faroe ridge (Beaird et al., 2013; Figure 1) by entrainment of Atlantic Waters by overflow waters originating from the Nordic Seas. Within the North Atlantic subpolar gyre, ISOW flows southward east of the Reykjanes Ridge in the Iceland Basin (e.g., Daniault et al., 2016; Fleischmann et al., 2001; McCartney, 1992; Zou et al., 2017; Figure 1). Most of the southward ISOW flow ultimately reaches the Irminger Sea through the Charlie-Gibbs Fracture Zone (CGFZ) near 52°N (Bower & Furey, 2017; Kanzow & Zenk, 2014; McCartney, 1992; Saunders, 1994) and the Bight Fracture Zone near 57°N (Lankhorst & Zenk, 2006; Petit et al., 2018; Xu et al., 2010; Figure 1). Along its southward pathway, ISOW interacts with North East Atlantic Deep Water (NEADW), an old water mass flowing northward in the eastern North Atlantic. NEADW results from a complex mixing between Lower Deep Water originating from around Antarctica and other surrounding water masses (van Aken, 2000). According to McCartney (1992), the intensity of the ISOW-NEADW interaction along the Reykjanes Ridge depends on whether NEADW circulates cyclonically in the Iceland Basin before entering the CGFZ with ISOW, or whether it follows a fairly direct route to the CGFZ with minimal looping in the Iceland Basin (McCartney, 1992; van Aken, 2000). The interaction between those two water masses within CGFZ and their relative contributions to the deep flow there has, however, never been documented.

Within the CGFZ, the mean westward ISOW transport was recently estimated at -1.7 ± 0.5 Sv from a 22-month-long current time series (Bower & Furey, 2017). This transport was subject to strong intraseasonal variability, with daily mean values ranging from -7.1 to $+3.0$ Sv (Bower & Furey, 2017). Large decreases in or even reversals of the westward ISOW transport were attributed to meanders of the eastward flowing North Atlantic Current (NAC) present at that time over the CGFZ and extending to depth greater than 2,500 m (Bower & von Appen, 2008; Bower & Furey, 2017; Saunders, 1994; Schott et al., 1999; Xu et al., 2018). According to Schott et al. (1999) and Bower and von Appen (2008), the westward ISOW flow was blocked by the NAC when its eastward surface velocity exceeded 15 cm/ s. Interestingly, the θ and S properties of ISOW were not modified during reversal (Bower & Furey, 2017) even though we could have expected some changes due either to the northward displacement of the deep water masses found below the NAC or to changes in the relative contribution between ISOW and NEADW. Indeed, the properties of the westward flow at CGFZ results from vertical and lateral mixing between ISOW, NEADW, and shallower waters (McCartney, 1992) and it could be expected that these mixing processes are modified when the NAC is located over the CGFZ.

After flowing through the CGFZ and Bight Fracture Zone, it is generally assumed that ISOW heads north in the Irminger Basin along the western flank of Reykjanes Ridge (Daniault et al., 2016). In the northern part of the Irminger Sea, ISOW merges with Denmark Strait Overflow Water (DSOW), a younger and denser water mass than ISOW, formed downstream of the Denmark Strait. In the Irminger Basin, ISOW and DSOW then flow southward within the Deep Western Boundary Current (DWBC), the major conduit for deep water masses to the subtropical gyre (Figure 1; Dickson & Brown, 1994; Daniault et al., 2016; McCartney & Talley, 1984; Saunders, 2001). Based on water mass property evolution or high resolution model simulations, other studies have suggested westward (McCartney, 1992; Smethie & Fine, 2001; Stramma et al., 2004) or northwestward (Xu et al., 2010) ISOW pathways between the CGFZ and the DWBC that bypass the circulation around the Irminger Sea. Xu et al. (2010) also suggested an eastward recirculation of ISOW across the southern valley of the CGFZ.

While ISOW plays a leading role in the storage of heat and anthropogenic carbon and their redistribution toward the rest of the ocean, there are still some uncertainties about the pathways of this water mass and how the climate signal that it carries is diluted by mixing with surrounding water masses. Based on ship-based and Argo hydrographic data as well as on surface dynamic conditions, we investigated the fate of ISOW, its interaction with NEADW and other surrounding water masses within the CGFZ and beyond, as well as its relationship with the NAC position. The ship-based hydrographic data were collected in the

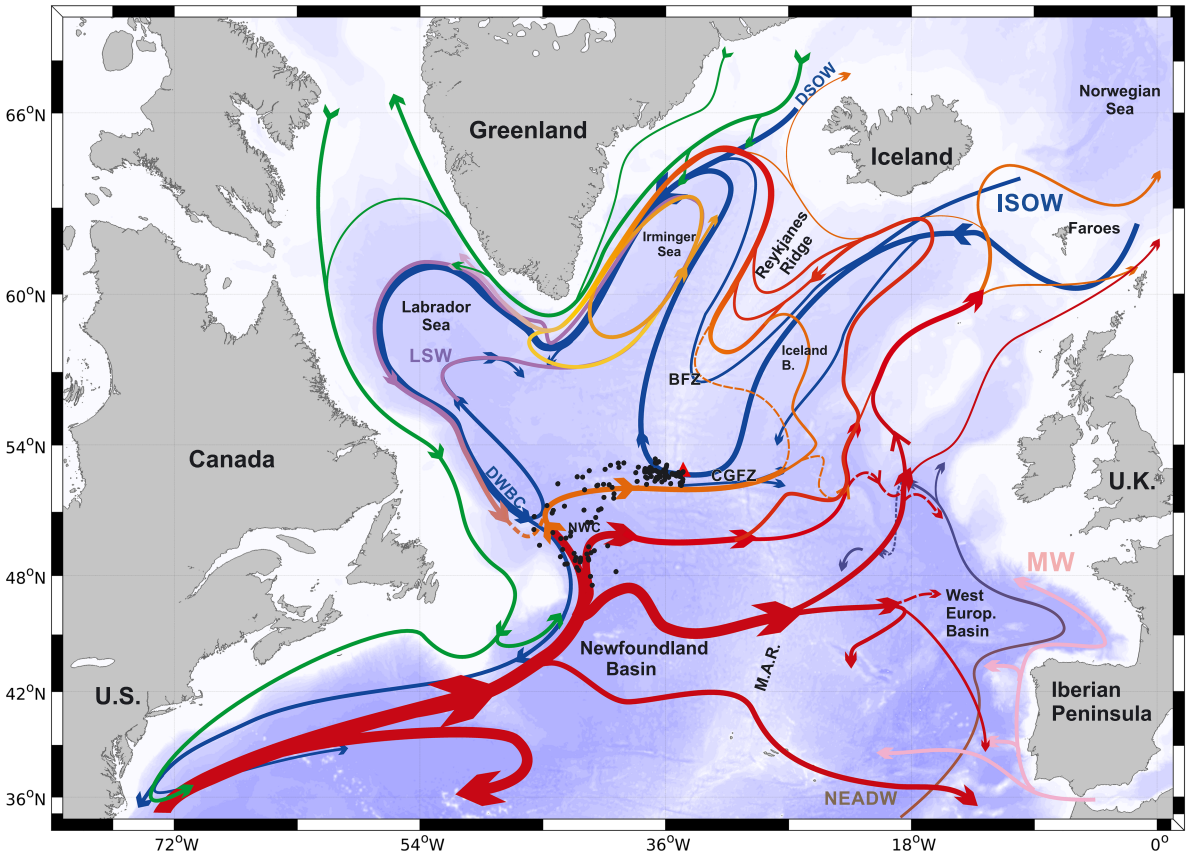

Figure 1. Schematic of the large-scale circulation of the North Atlantic Subpolar gyre from Daniault et al. (2016). Bathymetry is plotted in color, with isobaths at 100 m, 1,000 m, and every 1,000 m below 1,000 m. Deep circulation delimited by the isopycnal $\sigma_0 = 27.80$ is shown in blue. The North Atlantic Current is shown in red. Abbreviations indicate the Deep Western Boundary Current (DWBC), Labrador Sea Water (LSW), Iceland-Scotland Overflow Water (ISOW), Denmark Strait Overflow Water (DSOW), Mediterranean Water (MW), North East Atlantic Deep Water (NEADW), Meridional Atlantic Ridge (MAR), Charlie-Gibbs Fracture Zone (CGFZ), Bight Fracture Zone (BFZ), and North-West Corner (NWC). The orange triangle indicates the deployment position in the CGFZ of the five Deep-Argo floats. The black dots represent the position of the float profiles.

CGFZ in 2015 and 2017 as part of the French RREX (Reykjanes Ridge Experiment) project. Five Deep-Argo floats (0–4,000 m) equipped with temperature, salinity, and oxygen sensors were deployed in the CGFZ in 2015 and 2017 as part of the Novel Argo Observing System project. After presenting materials and methods in section 2, we will describe (section 3) and discuss (section 4) ISOW pathways and mixing inside and beyond the CGFZ.

2. Data and Methods

2.1. Deep-Arvor Float Data Set

The Deep-Argo floats used in this study are Deep-Arvor floats (Le Reste et al., 2016). They are capable of sampling the water column down to 4,000 m. Three Deep-Arvor floats were deployed simultaneously in the CGFZ (52.73°N to 35.08°W; Figure 2) on 3 July 2015 (DP15-1, DP15-2, and DP15-3) during the RREX2015 cruise (Branellec & Thierry, 2016; Petit et al., 2018). Two additional floats were also deployed at the same location on 9 August 2017 (DP17-1 and DP17-2) during the RREX2017 cruise (Branellec & Thierry, 2018; Table 1). Their respective World Meteorological Organization (WMO) codes are given in Table 1.

The five Deep-Arvor floats were programmed to drift at 2,750 dbar (referred to hereafter as the "parking depth") in the core layer of ISOW and every 10 days to measure profiles of temperature (T), salinity (S), and dissolved oxygen concentration (O_2) as a function of pressure (P) between 4,000 m or the bottom and the sea surface. The trajectory of the floats could have been influenced by currents encountered during their ascent and descent (about 12 hr each) and during surfacing for data transmission (about 10 min). However,

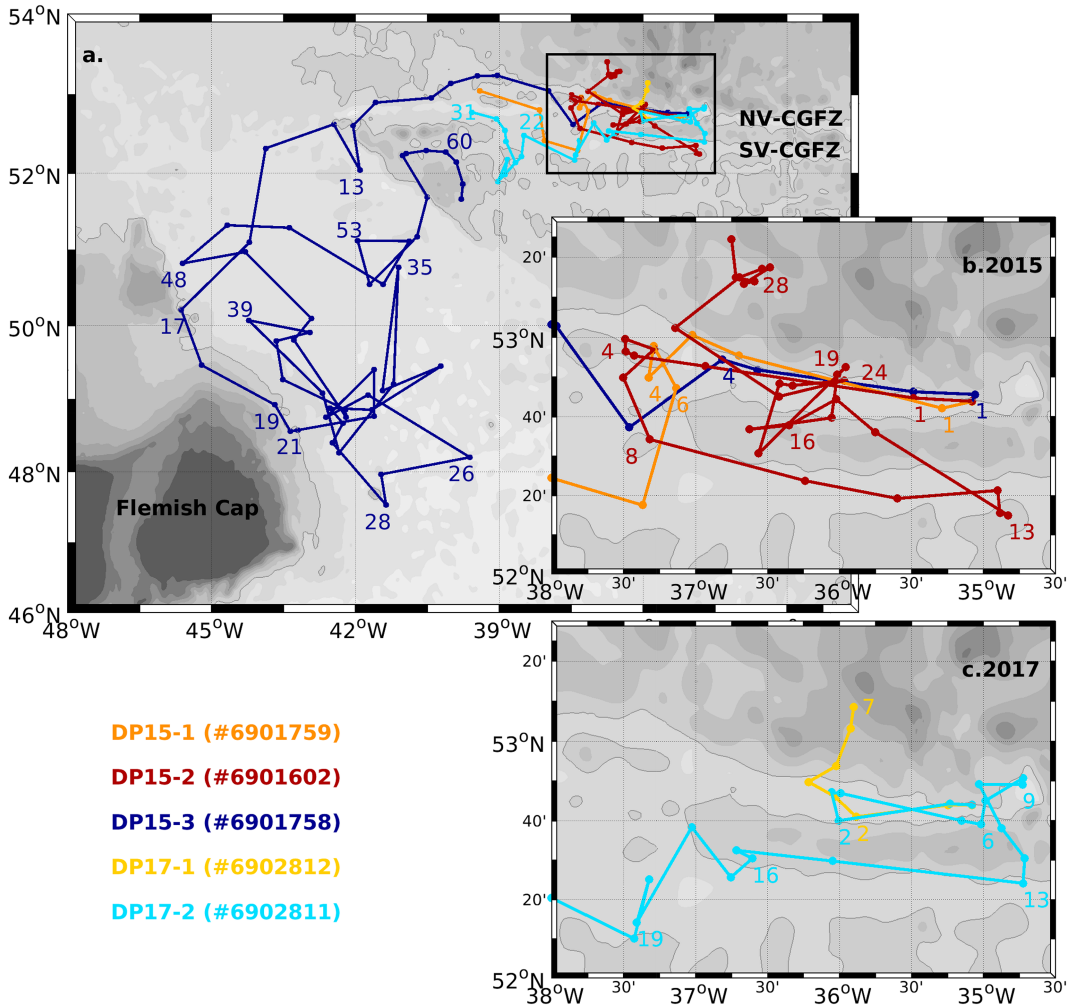

Figure 2. (a) Trajectories of the five Deep-Argo floats deployed in the Charlie-Gibbs Fracture Zone (CGFZ) in summers 2015 and 2017: DP15-1 (WMO#6901759) in orange; DP15-2 (#6901602) in red; DP15-3 (#6901758) in blue; DP17-1 (#6902812) in yellow; DP17-2 (#6902811) in cyan. (b, c) Zoom over the northern and the southern valleys (NV and SV) of the CGFZ for 2015 (b) and 2017 (c). Some cycle numbers where *P*, *T*, *S*, and O_2 profiles were collected are indicated. Bathymetry (m) is colored in gray (the darkest shade indicates the shallowest areas). The gray line shows the 3,500-m isobath.

Table 1
Information About the Five Deep-Argo Floats

Float ID	DP15-1	DP15-2	DP15-3	DP17-1	DP17-2
Float WMO	6901759	6901602	6901758	6902812	6902811
Deployment date		3 July 2015		9 August 2017	
Associated Cruise (reference CTD)		RREX15 (120)		RREX17 (109)	
End of life (number of cycles achieved)	10 October 2015 (10)	28 May 2016 (33)	24 March 2017 (63)	10 October 2017 (7)	Still active
Report on salinity data qualification			Cabanes et al. (2018)		
Report on O_2 data qualification			Gallian and Thierry (2018)		

Note. WMO = World Meteorological Organization; CTD = conductivity-temperature-depth. Dates are formatted as MM/DD/YYYY.

due to the bathymetric constraint imposed by the CGFZ, the eastward surface and subsurface currents are generally in the same vertical plane as the westward deep flow in the CGFZ, but in the opposite direction. As a consequence, the currents encountered during the float ascent or descent would only have led to an underestimation of the westward displacement of the float at its parking depth. Nonetheless, the float displacement was clearly influenced by surface or subsurface currents in some cases. This is further discussed in section 3.4, and the corresponding profiles were not used when we analyzed the water mass composition along the westward path of the floats (section 3.4). For some unexplained reason, DP15-2 and DP15-3 did not dive and drifted at the surface during their Cycle Number 18. Considering the topography of the area, the floats grounded at almost all cycles. Some of them suffered a premature "death" related to the management of the grounding by the float software. A new grounding management procedure has been implemented in recent Deep-Arvor floats to address this issue. It now allows the float to modify its parking depth if grounding occurs during the drifting phase. The new grounding procedure also allows the float to rise directly to the surface without waiting for the programmed ascending time if grounding occurs during descent to the profiling depth. No premature death was observed on the floats deployed in the subpolar gyre of the North Atlantic Ocean in 2018 with this new grounding procedure.

P, *T*, and *S* were measured using a SeaBird SBE41CP conductivity-temperature-depth sensor. Salinity bias was estimated based on the method proposed by Cabanes et al. (2016). This method, adapted from that of Owens and Wong (2009), is an objective analysis that compares the data obtained from a given float with a historical data set acquired in the area over the last 10 years for the 10 theta (θ) levels showing the least variability in salinity. Compared with Owens and Wong (2009), the modified method minimizes the contribution of the oldest historical data to account for the large interannual to decadal variability of the salinity field in the North Atlantic Ocean and provides more realistic error bars. Corrections proposed by the modified method and applied on our data set are detailed in Cabanes et al. (2018). These corrections were validated against an independent calibrated hydrographic profile acquired at float deployment (Table 1) and by comparing the profiles acquired in the CGFZ by the different floats in 2015 or 2017 (Figures S1–S5 in the supporting information). A negative pressure dependency of 1.5 x 10^{-6} $dbar^{-1}$ was recently detected on the SBE41 conductivity sensor (Kobayashi, 2019), which would lead to a fresh offset of about 0.007 at 4,000 dbar. In this study, the salinity bias was estimated from data measured in the deep layers. The potential effect of the pressure dependency on the salinity is thus not detectable in the deep layers, which are those investigated in this paper. It could lead to a salty anomaly of about 0.007 in the surface layers that yet lies within the measurement accuracy (0.01).

O_2 was measured at each profile with an Aanderaa Optode (4330), except for DP17-1 because the oxygen sensor failed. O_2 data were decoded following the Argo-O_2 processing manual (Thierry, Bittig, et al., 2018) and then corrected following the method of Takeshita et al. (2013). The data were first corrected for any temporal drift based on comparison to the World Atlas 2009 (Garcia et al., 2010). Then a correction was estimated by comparing the first ascending O_2 profile, expressed in terms of percent of saturation, with a calibrated reference profile acquired at the float deployment (Table 1). In some cases, the comparison between the corrected float profiles and the reference profile revealed the presence of a pressure-dependent bias, suggesting that the pressure correction proposed by Bittig et al. (2015) and taken into account during decoding was not sufficient. We thus applied an additional pressure correction to the raw data. The details of these corrections are provided in Gallian and Thierry (2018), and the corrected data are available in the Argo database (Figures S4 and S5).

Overall, the accuracy of temperature, salinity, and oxygen measurements was 0.01 °C, better than 0.01, and 2.5 μmol/ kg, respectively.

2.2. Optimum Multiparameter Analysis

An Optimum Multiparameter (OMP) analysis was used to identify water masses that explain hydrological and biogeochemical properties measured by the Deep-Argo floats near their parking depths. This method, introduced by Tomczak (1981) and extended by the OMP user group from GEOMAR (http://omp.geomar.de/), is based on a simple model of linear mixing between predefined source water types (SWTs). It assumes that mixing coefficients are identical for all SWT properties. The fraction of each SWT (xi) is determined through the following set of linear mixing equations (equations (1)–(3)) written here for three SWTs defined by their potential temperature (θ_1 to θ_3), salinity (S_1 to S_3) and dissolved oxygen concentration ($O_{2,\,1}$ to $O_{2,\,3}$)

and for a water mass (WM) conservation equation (equation (4)) for which residuals (R) are minimized in a nonnegative least squares sense. The subscript obs refers to the float observations that we want to explain as the sum of the SWT fractions.

$$x_1\theta_1 + x_2\theta_2 + x_3\theta_3 = \theta_{\text{obs}} + R_\theta \tag{1}$$

$$x_1S_1 + x_2S_2 + x_3S_3 = S_{\text{obs}} + R_S \tag{2}$$

$$x_1\text{O}_{2,1} + x_2\text{O}_{2,2} + x_3\text{O}_{2,3} = \text{O}_{2,\text{obs}} + R_{\text{O2}} \tag{3}$$

$$x_1 + x_2 + x_3 = 1 + R_{\text{WM}} \tag{4}$$

The interpretation of the mixing coefficients depends on the selection criteria for the SWTs (Tomczak, 1981). In this study, SWTs were defined directly from our Deep-Argo data set (section 3.2) to investigate regional mixing instead of mixing between SWTs from remote formation regions. The advantage of this definition is that only a few parameters are necessary to resolve the OMP analysis because local water type properties are little influenced by remineralization. Otherwise, nutrients, which were not measured by our deep float, would have been needed to account for this biologihttp://omp.geomar.de/). We will thus use the more appropriate term Local Water Type (LWT) instead of SWT hereinafter.

To account for the new deep ventilation events recorded in winters 2015 and 2016 in the Irminger and Labrador Seas (de Jong & de Steur, 2016; Piron et al., 2017; Yashayaev & Loder, 2016), we performed two OMP analyses based on the data acquired either by the floats deployed in 2015 or those deployed in 2017. For each OMP analysis, the θ, S, and O_2 values of the LWTs were defined from the ship-based and Deep-Argo data (section 3.2 and Table 2). Planetary potential vorticity was not considered as an additional tracer here because it is not conservative in the NAC region due to large relative vorticity. Because LWTs are defined by three tracers, the mixing model has four equations (equations (1)–(4)) and one observation can be explained by the mixing between at most three LWTs. To estimate LWT fractions explaining observations near the float parking depth (2,750 dbar), different mixing configurations of two or three LWTs were tested. Results presented in sections 3.3 and 3.4 correspond to the LWT mixing configuration that minimizes ROMP defined as follows:

$$R^{\text{OMP}} = \frac{R_\theta^2}{s_\theta^2} + \frac{R_S^2}{s_s^2} + \frac{R_{\text{O2}}^2}{s_{\text{O2}}^2} + R_{\text{WM}}^2 \tag{5}$$

where ${R_\theta}^2$, ${R_S}^2$, ${R_{O2}}^2$, and ${R_{WM}}^2$ are the model residuals and S_θ, S_S, and S_{O2} are the standard deviations computed from the properties of the LWT; θ, S, and O_2 of the LWT, characterized by different environmental variabilities or instrumental and analytical accuracies. To account for this variability, Tomczak and Large (1989) proposed to weight equations (1)–(3) based on the relation between the standard deviation of the properties of each LWT (Table 2) and the largest variance of the parameter in the source regions. Here, to obtain comparable results from all mixing configurations tested in this study, we prefer to fix the ratio $\theta/S/O_2$/mass conservation to weight equations (1)–(4). We used the ratio 3/ 1/1/3 that gives less weight to salinity and oxygen whose sensors were less accurate than the temperature sensor.

The OMP analysis was performed for each measurement of every vertical profile of every float. The results were then interpolated on selected isopycnals (see sections 3.2 and 3.4).

3. Results

3.1. Trajectories of Deep Floats

During the first month, the three floats deployed simultaneously in July 2015 (Table 1) moved westward in the northern valley of the CGFZ (Figures 2a and 2b). Between 37°W and 37.5°W (53°N), the three floats were apparently blocked in their westward displacement and changed direction. After three chaotic cycles with different flow directions (Cycles 4–6), DP15-1 moved southward before heading west and dying, whereas DP15-2 recirculated eastward in the southern valley of the CGFZ (from Cycle 8 to Cycle 13). At 35°W (52.25°N), south of its deployment position, DP15-2 headed northwest back to its initial trajectory. During

Table 2
Local Water Types (LWT) Used to Resolve the OMP Analysis

Name	In 2015		In 2017	
LWT1: ISOW Iceland-Scotland Overflow Water	(θ) 2.89 ± 0.04 °C	(32)	2.80 ± 0.05 °C	(5)
	(S) 34.981 ± 0.000		34.978 ± 0.000	
	(O_2) 273.2 ± 0.2 μmol/kg		274.0 ± 0.2 μmol/kg	
LWT2: IW Intermediate Water	(θ) 4.40 ± 0.06 °C	(55)	4.38 ± 0.05 °C	(33)
	(S) 34.934 ± 0.006		34.927 ± 0.003	
	(O_2) 268.8 ± 2.6 μmol kg^{-1}		262.2 ± 1.2 μmol/kg	
LWT3: LSW Labrador Sea Water	(θ) 3.42 ± 0.03 °C	(74)	3.35 ± 0.03 °C	(51)
	(S) 34.876 ± 0.002		34.878 ± 0.001	
	(O_2) 291 ± 1.0 μmol/kg		290.6 ± 0.7 μmol/kg	
LWT4: DSOW Denmark Strait Overflow Water	(θ) 1.92 ± 0.03	(74)	Not detected	
	(S) 34.908 ± 0.005			
	(O_2) 287.1 ± 1.7 μmol/kg			
LWT5: DSOWi interior route of Denmark Strait Overflow Water	(θ) 1.85 ± 0.01 °C	(32)	2.15 ± 0.03 °C	(12)
	(S) 34.899 ± 0.000		34.911 ± 0.002	
	(O_2) 283.4 ± 0.2 μmol/kg		275.3 ± 0.5 μmol/kg	
LWT6: NEADW North East Atlantic Deep Water	(Θ) 2.61 ± 0.04 °C	(55)	2.58 ± 0.00 °C	(34)
	(S) 34.956 ± 0.005		34.959 ± 0.001	
	(O_2) 268.6 ± 0.3 μmol/kg		264.8 ± 0.0 μmol/kg	
LWT7: DW deep water	(θ) 3.49 ± 0.07 °C	(63)	Not detected	
	(S) 34.936 ± 0.002			
	(O_2) 271.2 ± 0.3 μmol/kg			

Note. Each LWT core is defined by a potential temperature (θ), salinity (S), and dissolved oxygen concentration (O_2) value calculated from the float data set as detailed in section 3.2. The standard deviation and number of data (in brackets) used to calculate the averaged values are given for information.

the next three months, its displacement was chaotic and remained between 36°W and 37°W in the northern valley of the CGFZ. At Cycle 24, 6 months after its deployment, DP15-2 was still in the northern valley and moved westward for two cycles until 37°W (53°N) where it turned northeastward toward the Irminger Basin. It died 2 months later. Meanwhile, DP15-3, which deviated to the south from its westward displacement at the same time as the two other floats (namely, at Cycle 4), but upstream (east of 37°W), came back to a westward displacement in the northern valley (Figure 2a). After exiting the CGFZ at 38°W, DP15-3 continued toward the southwest to reach the Newfoundland Basin 4 months later (Cycles 17–18). It then circulated southward along the Flemish Cap during two cycles (Cycles 19–20), before moving with an apparent chaotic progression through a large area (46–39°W/47.5–52.5°N; Figure 2a) dominated by the NAC (Figure 1).

The two floats launched simultaneously in August 2017 (Table 1) at the same position as those deployed in 2015 also moved westward in the northern valley of the CGFZ over their first cycles (Figures 2a and 2c). Their westward trajectories were also disrupted but at a more eastern longitude (36°W) compared with 2015 (37.5°W). From 36°W, DP17-1 headed north for 1 month and died, whereas DP17-2 recirculated eastward in the northern valley back to its initial position (Cycle 6). It then moved with a chaotic progression around the meridian 35°W (Figure 2c) before reaching the southern valley of the CGFZ (Cycle 13). Inside the southern valley, DP17-2 quickly moved westward along the northern wall of the valley (Cycles 13 to 16) and left the CGFZ after Cycle 19. Beyond the CGFZ, DP17-2 continued westward toward the western part of the subpolar gyre. Its trajectory was more south and more disrupted than that of DP15-1 and DP15-3 (Figure 2a). At each of these disruptions (37.5°W and 39°W), DP17-2 followed a southward-northward displacement before returning back to its initial westward trajectory. Data acquired after 7 June 2018 (Cycle 31) are not presented in this study.

To sum up, the five deep floats generally moved westward during their stay in the CGFZ, in particular during the first few cycles after their deployment. This overall westward displacement was perturbed between 36°W and 38°W, where some floats moved northward, southward or recirculated eastward in the southern or the northern valley without going east of 34.5°W. Finally, two floats (DP15-3 and DP17-2) made measurements beyond the CGFZ, and one of these reached the Newfoundland basin and drifted in the area dominated by the NAC.

3.2. Hydrological and Biogeochemical Properties Measured by Deep Floats: LWT Definition

This section aims to define the set of LWTs used in the OMP analysis (section 2.2) that best explains the evolution of θ, S, and O_2 properties measured by the deep floats along their trajectories. The potential temperature, salinity, and dissolved oxygen concentration sections show the main water masses sampled by the floats along their paths (Figures 3–5). The water masses used as LWTs in the OMP analysis are described below, and their θ, S, and O_2 properties are summarized in Table 2. The float profiles used to define these properties are shown in Figures 6 and 7.

ISOW or LWT1. ISOW is observed below 27.80 σ_0. Its core is characterized by a deep salinity maximum near 2,750 m (Saunders, 1996), with values ranging between 34.96 (Schott et al., 1999) and 34.99 (Worthington & Volkmann, 1965). A deep salinity maximum of 34.98 was measured by Deep-Argo floats near their parking depth over their first cycles (Figures 3–5). A ship-based hydrographic section was made across the CGFZ during the RREX cruises and provides a more complete view of the ISOW properties at float deployment time (Figure 6). To define the first LWT, we thus averaged θ and O_2 values from the RREX data set for which salinity below 27.80 σ_0 in the CGFZ was maximum (S_{max} = 34.981 for stations 117 to 122 for the RREX15 cruise and S_{max} = 34.978 for stations 106 to 110 for the RREX17 cruise; Figure 6 and Table 2). Here, the ISOW core was detected at σ_2 = 37.03 kg/ m^3 ($\sigma_0 \approx$ 27.88 kg/ m^3; Figure 6) and characterized by salinities comparable to those reported by Bower and Furey (2017) in 2010–2012 for the northern valley of the CGFZ (maximum mean salinities of 34.975).

IW or LWT2. Intermediate Water (IW) is a low-oxygenated water mass observed in the upper 1,000 m of the water column and originating from the eastern subpolar gyre (Harvey & Arhan, 1988; van Aken & de Boer, 1995). It was observed during the RREX2015 cruise along the Reykjanes Ridge between 27.52 σ_0 and 27.71 σ_0 (Petit et al., 2018). At this density range, IW differs from the other water masses by having an oxygen concentration lower than 272 μmol/ kg (Petit et al., 2018). IW was sampled at the CGFZ by the deep floats launched during RREX2015 and RREX2017 (Figures 3 and 7). Here, its averaged θ, S, and O_2 values were estimated from the low oxygen concentration (<272 μmol/ kg) detected by the deep floats between 27.68 σ_0 and 27.7I σ_0 (Table 2 and Figure 7).

LSW or LWT3. LSW is formed in winter by deep convection in the Labrador and Irminger Seas (de Jong & de Steur, 2016; Piron et al., 2017; Våge et al., 2011; Yashayaev & Loder, 2016). It spreads eastward through the subpolar gyre and southward toward the subtropical gyre within the DWBC (McCartney & Talley, 1982; McCartney, 1992; Sy et al., 1997; Talley & McCartney, 1982). LSW is the freshest (<34.89) and most oxygenated (>280 μmol/ kg) water mass detected between 27.68 σ_0 and 27.80 σ_0 in this region (Dickson et al., 1996; Lazier, 1973; Yashayaev, 2007). Figures 3–5 show that LSW was regularly sampled by the deep floats both in the CGFZ area and in the Newfoundland Basin. The averaged θ, S, and O_2 values of this third LWT were estimated from the deep float data set measured between 27.68 σ_0 and 27.80 σ_0, with salinity lower than 34.88 and oxygen concentrations higher than 290 μmol/ kg (Figure 6). Properties of this LWT core (Table 2) were estimated from the most westerly measurements made by DP15-3 in 2015 (Cycles 13, 15, 16, 20, and 21; Figures 5 and 6) and by DP17-2 in 2017 (Cycles 21, 26, 28, and 29; Figures 4 and 6 and Table 2), to be as close as possible to the LSW formation area.

DSOW and DSOWi or LWT4 and LWT5. DSOW flows southward in the Irminger Sea and the Labrador Sea within the DWBC. DSOW is the coldest and the densest water mass of the western subpolar gyre (Kieke & Rhein, 2006) characterized by oxygen concentrations higher than 280 μmol/ kg (e.g., Falina et al., 2012; Tanhua et al., 2005). Oxygen sections from floats deployed in 2015 reveal high oxygen concentrations below 3,000-m depth (below 27.88 σ_0; Figures 3–5). Maximum values (>284 μmol/ kg) were detected by DP15-3 northeast of Flemish Cap at 49°N to 44°W (Cycles 19–21; Figures 5 and 6). This deep maximum in oxygen concentration was characterized by a potential temperature lower than 2 °C and by salinity values slightly higher than 34.90 (Table 2 and Figures 5 and 6). This is consistent with past studies that showed salinity of DSOW in the DWBC at Flemish Cap to range between 34.89 and 34.91 (Mertens et al., 2014; Stramma et al., 2004). Averaged properties associated with the deep oxygen maximum (O_2 > 284 μmol/ kg below 27.88 σ_0) measured by DP15-3 were thus used to define the fourth LWT (Table 2). This definition was, however, inadequate to solve the OMP analysis of all profiles of DP15-3 with reasonable residuals. Residuals of salinity, oxygen, and potential temperature measured in the region dominated by the NAC

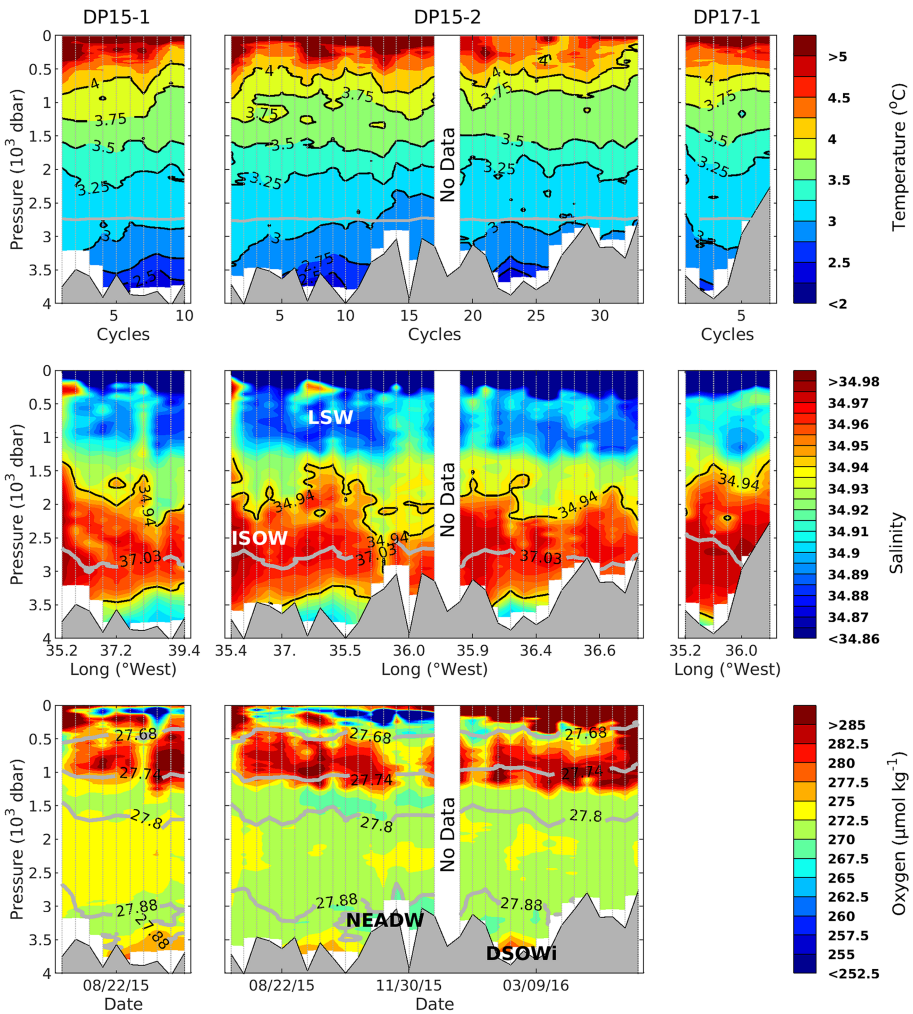

Figure 3. Section of potential temperature (top row; °C), salinity (middle row), and dissolved oxygen concentration (bottom row; µmol/kg) measured in the CGFZ by DP15-1 (left panels), DP15-2 (middle panels), and by DP17-1 (right panels). Black lines on the potential temperature section represent isotherms 2.5 to 4 °C with 0.25 resolution, whereas those on the salinity section represent isohaline 34.94 below 27.80 σ_0. Vertical dotted gray lines on the three panels represent float profiles. Thick gray lines indicate the parking depth on the potential temperature section, the $\sigma_2 = 37.03$ isopycnal on the salinity section, and the $\sigma_0 = 27.68$, 27.74, 27.80 and 27.88 isopycnals on the oxygen section. The following local water types used in the Optimum Multiparameter analysis are indicated: Iceland-Scotland Overflow Water (ISOW), Labrador Sea Water (LSW), North East Atlantic Deep Water (NEADW), and interior Denmark Strait Overflow Water (DSOWi). Filled gray areas show the bathymetry.

(from Cycle 20) were in fact higher than the accuracy measurements. Such residuals suggested that a fifth LWT was needed to complete our model (section 2.2). The θ-S-O_2 diagram from DP15-3 (Figure 6) shows a second oxygen maximum (>282 µmol/ kg) at the DSOW layer, but with salinity values lower than 34.90. It was detected west of 42°W between 52°N and 53°N at Cycles 14 and 15 (Figure 5). These conditions (S < 34.90 and O_2 > 282 µmol/ kg below 27.88 σ_0) were used to define the averaged θ, S, and O_2 properties of a fifth LWT (Table 2), allowing the OMP analysis to be successfully completed. Averaged salinity of this LWT (34.899 ± 0.000; Table 2) is within the salinity range of 34.89 to 34.91 reported by Stramma et al. (2004) and by Mertens et al. (2014). This water mass, which properties can be explained by the influence of shelf water cascading down to DSOW layer and by its recirculation in the Newfoundland basin, will be called interior DSOW (DSOWi) hereafter. Indeed, dense Greenland shelf water cascading down to the DSOW layer can cause a freshening and an increase in oxygen of the DSOW (Falina et al., 2007). As DSOWi is fresher than DSOW but not more oxygenated, the lower oxygen concentration would

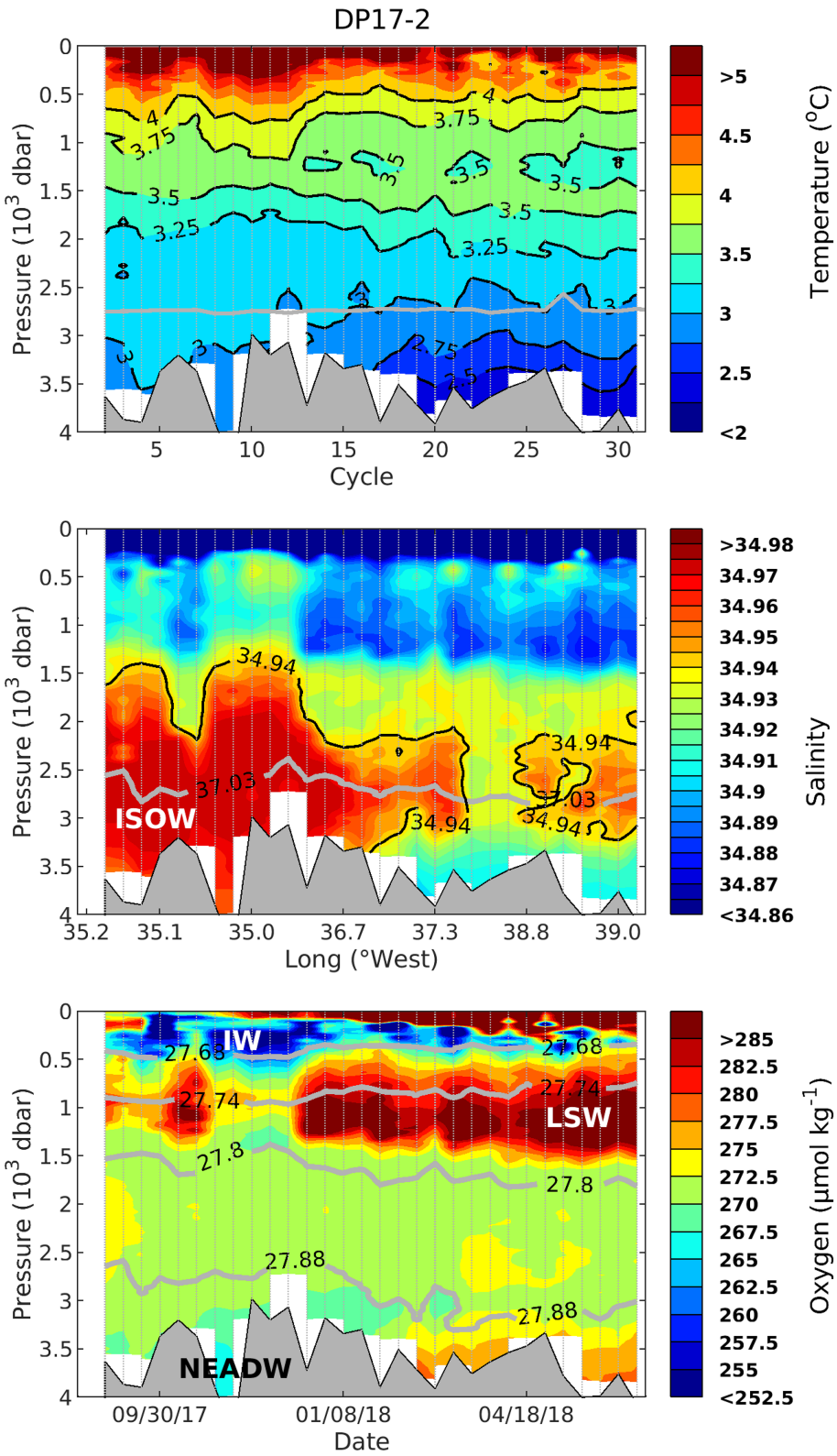

Figure 4. Same as Figure 3, but for DP17-2. The following local water types used in the Optimum Multiparameter analysis are indicated: Iceland-Scotland Overflow Water (ISOW), Intermediate Water (IW), Labrador Sea Water (LSW), and North East Atlantic Deep Water (NEADW).

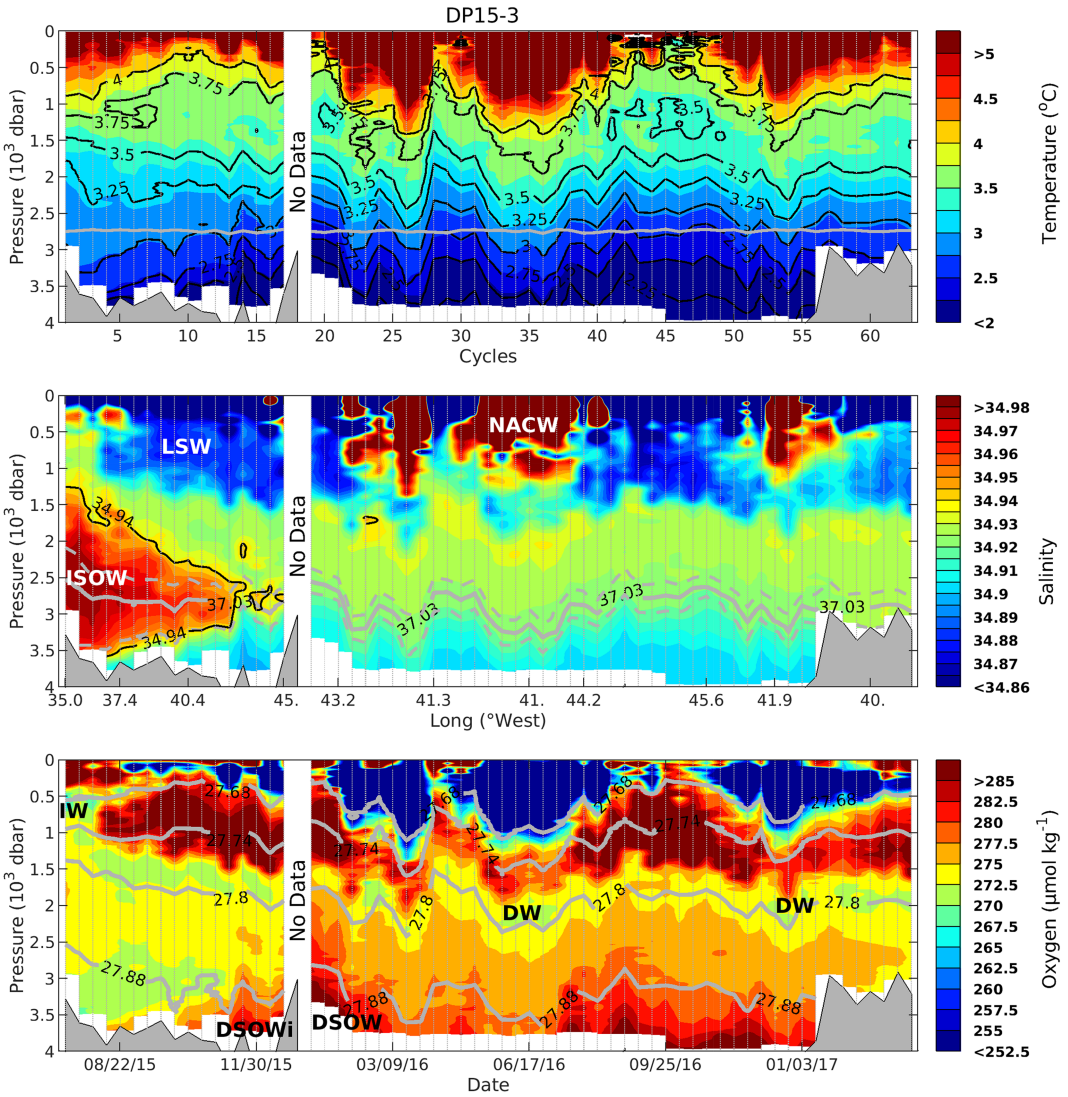

Figure 5. Same as Figure 3, but for DP15-3. The following local water types used in the Optimum Multiparameter analysis are indicated: Iceland-Scotland Overflow Water (ISOW), Intermediate Water (IW), Labrador Sea Water (LSW), Deep Water (DW), Denmark Strait Overflow Water (DSOW), and interior DSOW (DSOWi) as well as North Atlantic Central Water (NACW), illustrating the North Atlantic Current position. Gray dashed lines on the salinity section represent the 37.01σ_2 and 37.05 σ_2 isopycnals.

result from the DSOW recirculation in the interior basin and its mixing with the Lower Deep Water originating from the subtropics that is saltier and less oxygenated than DSOW (see Figure 9.15 in Talley et al., 2011). The area sampled by the two floats deployed in 2017 was limited to the CGFZ. In this context, DSOW (LWT4) was not detected in 2017, whereas DSOWi (LWT5) was defined from the coldest and most oxygenated water mass detected there (Figure 6).

NEADW or LWT6. NEADW is an old water mass of southern origin characterized by low oxygen concentrations (van Aken & Becker, 1996) and easily identifiable from its linear relationship in θ-S diagram (Mantyla, 1994; Saunders, 1986). Such a linear θ-S relationship with low oxygen concentrations (between 265 and 269 µmol/ kg) is visible on the RREX profiles sampled in 2015 and 2017 in the CGFZ just below ISOW (Figure 6, LWT1). It is also observed from data measured in the northern and southern valleys of the CGFZ by DP15-2 (Cycle 12 to 15), DP15-3 (Cycle 2), and DP17-2 (Cycle 8; Figures 3–5 and 7). This attests that NEADW was sampled by the Deep-Argo floats in the CGFZ. We thus used NEADW as the sixth LWT to resolve the OMP analysis. The S-O_2 diagram of DP15-2 (Cycle 12 to 15), DP15-3 (Cycle 2), and DP17-2

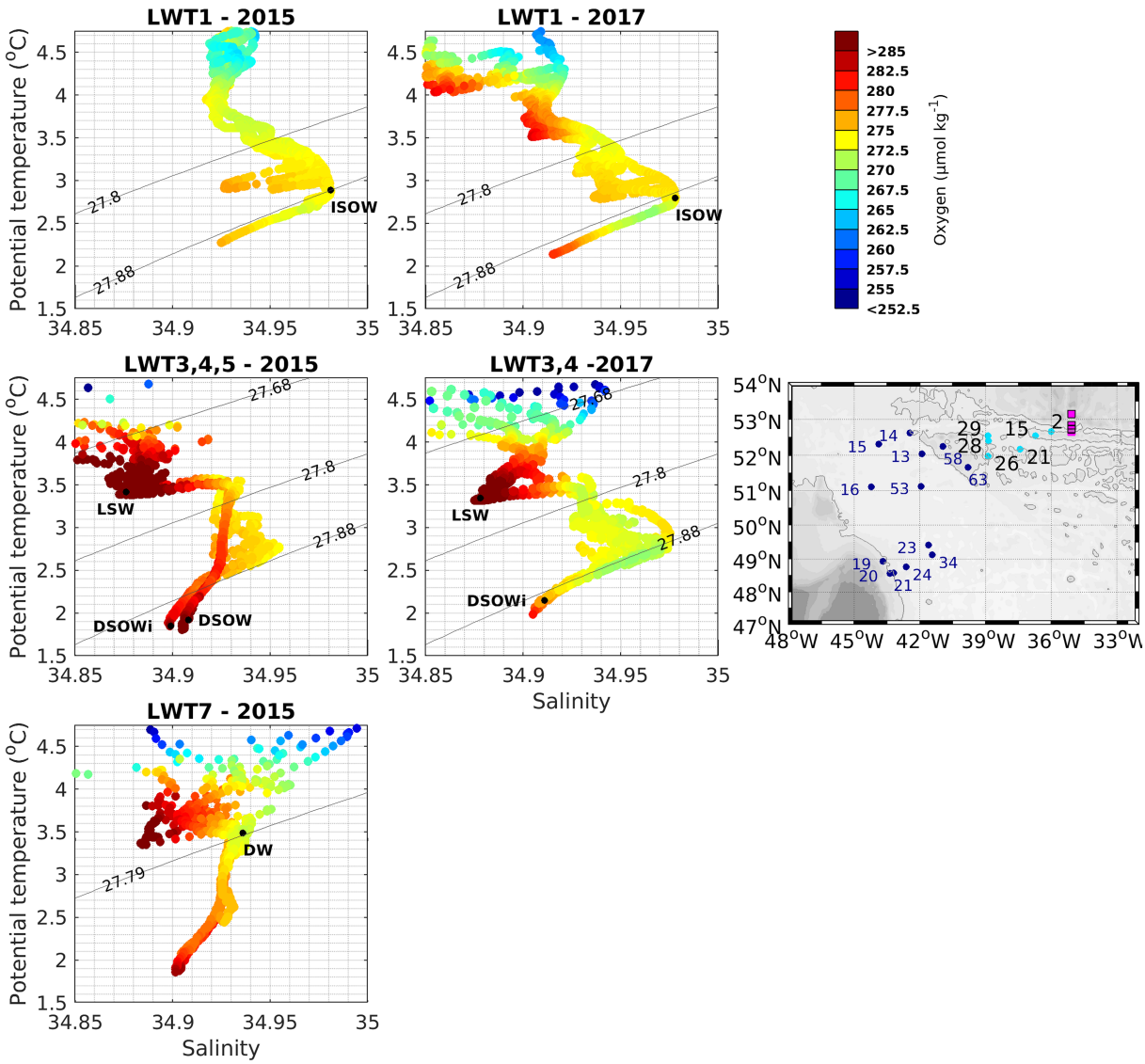

Figure 6. (a–e) The θ/S diagrams of the profiles used to define the properties of the local water types (LWTs) for the Optimum Multiparameter analysis. In each panel, the black dot indicates the position of the LWT in the diagram and the black line with a number shows the isopycnal σ_0 of interest. The color represents dissolved oxygen concentration (µmol/kg). (f) Position of the profiles displayed on panels (a–e). Bathymetry (m) is colored in gray (the darkest shade indicates the shallowest areas). The gray line shows the 3,500-m isobath. ISOW (LWT1) in 2015 (a) is defined from Stations 117 to 122 during the RREX15 cruise (magenta squares on panel f). In 2017, ISOW (b) is defined from stations 106 to 110 during the RREX17 cruise (black squares on panel f). LSW (LWT3) in 2015 (c) is defined from Cycles 13, 15, 16, 20, and 21 of DP15-3 (blue dots on panel f). LSW in 2017 (d) is defined from Cycles 21, 26, 28, and 29 of DP17-2 (cyan dots with black numbers). DSOW (LWT4) and DSOWi (LWT5) in 2015 (c) are defined from Cycles 19, 20, and 21 and from Cycles 14 and 15 of DP15-3 (blue dots on panel f), respectively. In 2017, DSOWi (d) is defined from Cycles 2 and 15 of DP17-2 (cyan dots with black numbers on panel f). Deep water (DW, LWT7) in 2015 (e) is defined from Cycles 23, 24, 34, 53, 58, and 63 of DP15-3 (blue dots on panel f). ISOW = Iceland-Scotland Overflow Water; DSOW = Denmark Strait Overflow Water; DSOWi = interior DSOW; DW = deep water; LSW = Labrador Sea Water.

(Cycle 8; Figure 7) for data measured below 27.80 σ_0 shows that the core of this sixth LWT is characterized by an oxygen minimum. Its averaged θ, S, and O_2 properties (Table 2) were thus calculated from data with $\sigma_0 < 27.80$ kg/ m^3 for which the oxygen concentration was lower than 269 µmol/ kg. The $\theta/S/O_2$ characteristics selected here for the LWT6 are consistent with those of the upper NEADW used by Garcia-Ibanez et al. (2015) for their OMP analysis along the Greenland-Portugal OVIDE section.

DW or LWT7. Finally, to complete the OMP analyses of DP15-3 in the western region dominated by the NAC, we needed to define a seventh LWT. Its averaged θ, S, and O_2 values were estimated by considering the

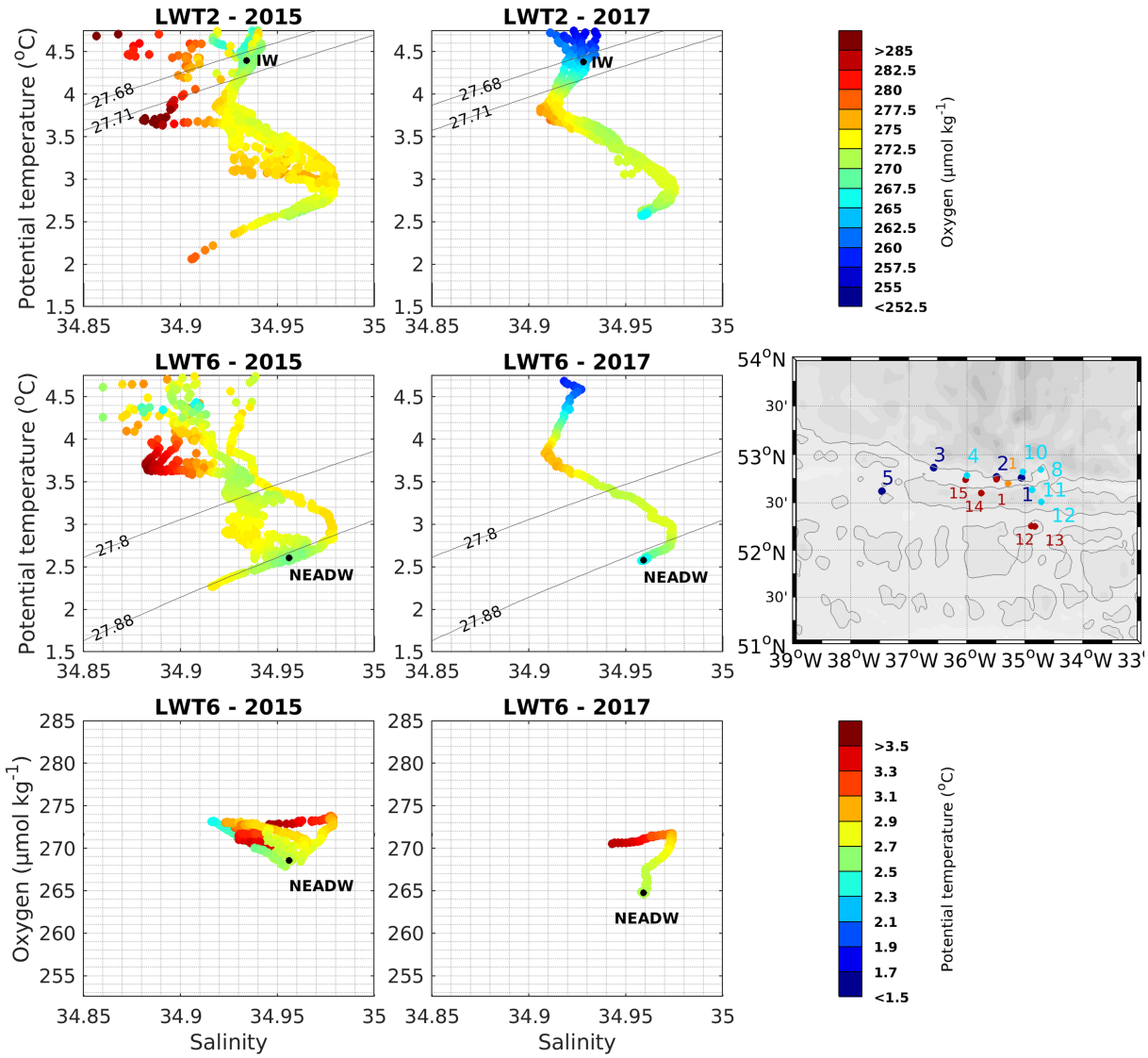

Figure 7. (a–d) The θ/S diagrams and (e–f) O_2-S diagrams of the profiles used to define the properties of the local water types (LWTs) for the Optimum Multiparameter analysis. In each panel, the black dot indicates the position of the LWT in the diagram and the black line with a number shows the isopycnal σ_0 of interest. On panels a–d, the color represents dissolved oxygen concentration (µmol/kg), whereas on panels e–f it represents the potential temperature (°C). (g) Position of the profiles displayed on panels a–f. Bathymetry (m) is colored in gray (the darkest shade indicates the shallowest areas). The gray line shows the, 3500-m isobath. IW (LWT2) in 2015 (a) is defined from Cycle 1 of DP15-1 (orange dots on panel g), Cycle 1 of DP15-2 (red dots on panel g), and Cycles 1–3 and 5 of DP15-3 (blue dots on panel g). In 2017, IW (b) is defined from Cycles 4, 8, 10, 11, and 12 of DP17-2 (cyan dots on panel g). NEADW (LWT6) in 2015 (c–e) is defined from Cycles 12–15 of DP15-2 (red dots on panel g) and Cycle 2 of DP15-3 (blue dots on panel g). NEADW in 2017 (d–f) is defined from Cycle 8 of DP17-2 (cyan dots on panel g). IW = intermediate water; NEADW = North East Atlantic Deep Water.

oxygen minimum (<272.5 µmol/ kg) sampled by the float during Cycles 23, 24, 34, 53, 58, and 63 (Figures 5 and 6). This oxygen minimum, detected along isopycnal 27.79 σ_0, is associated with salinity ranging from 34.93 to 34.94 (Figure 6). This water mass corresponds to the North West Atlantic Deep Water identified by Harvey and Arhan (1988) on the western side of the Mid-Atlantic Ridge during the TOPOGULF experiment. To avoid confusion with NEADW, we use the term of Deep Water (DW) hereinafter.

To summarize, we defined five LWTs (ISOW, IW, LSW, NEADW, and DSOWi) to explain the evolution of θ, S, and O_2 properties of deep water masses measured by the five Deep-Arvor floats in the CGFZ and beyond, and two additional LWTs (DW and DSOW) for the region dominated by the NAC that was only sampled by DP15-3.

3.3. Composition of Deep Flow in the CGFZ

This section focuses on the OMP results in the CGFZ area, which is to say is between 38°W and 34.5°W (Figure 2), and on $\sigma_2 = 37.03$ kg/ m^3, the density level where ISOW core was detected during the float deployment period (section 3.2; Figures 3 and 5). Note that OMP results provide information about the relative proportion of two or three LWTs explaining θ, S, O_2 properties observed on a given density level but not on the volume of each water mass. We used OMP results to investigate whether ISOW mixes with other water masses while flowing within CGFZ, particularly when the NAC moves northward above the CGFZ. Indeed, Bower and Furey (2017) showed that the strong interaction between the NAC and ISOW flows in the CGFZ did not change the θ-S properties of ISOW. Oxygen acquisition by our deep floats allowed us to test whether this hypothesis also holds for biogeochemical properties.

To investigate the NAC influence on water mass transport at the ISOW level, we built on the result from Bower and von Appen (2008) according to which the westward ISOW deep flow is disrupted by deep reaching velocities of the NAC when its eastward surface velocity exceeds 15 cm/ s. In this context, we analyzed the water mass composition on the 37.03 σ_2 isopycnal as a function of the float position and that of the NAC with surface velocities higher than 15 cm/ s. Note that in the following the NAC refers to meanders and eddies belonging to the whole NAC system that were observed at or near the CGFZ with surface velocities higher than 15 cm/ s.

OMP results and surface velocities were thus averaged over given periods characterized by specific positions of the NAC with respect to the CGFZ (Figures 8–10). Corresponding θ, S, and O_2 residuals are shown in Figure S6.

The expected case is that for which water mass properties on the 37.03 σ_2 isopycnal are mainly explained by those of ISOW. Such a situation was observed in the first month after float deployment in 2015 and 2017 (Figure 8). Mean OMP results show that θ-S-O_2 properties measured at 37.03 σ_2 by the floats result from a mixing of 85 ± 10% (88 ± 6%) ISOW, 13 ± 10% (7 ± 8%) NEADW, and 1 ± 1% (2 ± 3%) LSW in 2015 (2017). At that time, all floats moved westward in the northern valley of the CGFZ and the surface eastward currents were weak enough not to influence the deep westward flow or the trajectory of the floats very much (Figures 2 and 8, left). ISOW was also identified as the major water mass explaining properties observed on the 37.03 σ_2 isopycnal when DP15-2 came back to the northern valley of the CGFZ six months after its deployment (Cycles 19–20 near 36°W, OMP results not shown; see Figure 2). During all those periods, the floats were located in the northern valley of CGFZ and the NAC was located above the southern valley of the CGFZ, that is, south of the float position (Figure 8, left).

Apart from this case, where ISOW contributed more than 85%, a range of various other configurations was also observed with a larger proportion of NEADW (Figures 9 and 10). The data suggest that the NEADW contribution increases south of the northern valley or when the NAC moves northward. For instance, with a similar position of the NAC above the southern valley of the CGFZ as in the expected case, the relative proportion of NEADW increased to 40% or even 70% when the floats were located either in between the two valleys (Figure 9, top) or in the southern valley (Figures 9 and 10, bottom). Note that in those configurations, either the deep float moved westward in the opposite direction to the upper current (Figure 9, top) or the float was stopped or moved eastward underneath the NAC. On the contrary, with a similar float position in the northern valley as in the expected case (Figure 10, top and middle), the relative contribution of NEADW increased to about 50% when a NAC meander or eddy reached the northern valley (see meander at 37°W in Figure 10, top; or eddy located at 38.9°W and 53.5°N on Figure 10, middle).

Finally, the OMP results show that the two main water masses that contributed to the θ-S-O_2 properties on the 37.03 σ_2 isopycnal in the CGFZ were ISOW and NEADW (Figures 8–10). The situations sampled by the floats show that the relative contribution of ISOW (NEADW) varied between about 15% and 90% (10% and 85%) and that the third contributing water mass was LSW (less than 10%). They suggest that ISOW was prevailing (more than 85%) in the deep westward flow in the northern valley of CGFZ when the NAC was south of this valley. The NEADW contribution was quantified to more than 40% in between the two valleys of the CGFZ, in the southern valley, and in the northern valley of CGFZ when a NAC meander or eddy was located there.

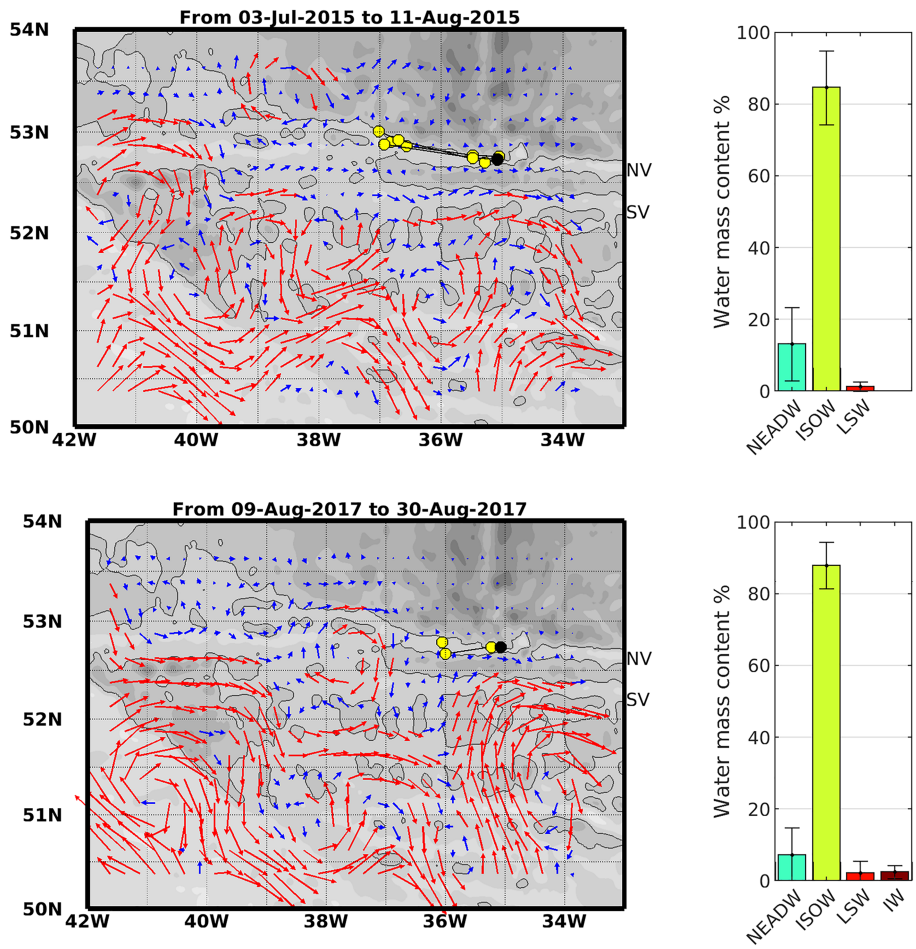

Figure 8. (left panels) Satellite-derived surface velocities (arrows) from AVISO (daily resolution, ¼°) averaged (top) from 3 July to 11 August 2015 and (bottom) from 9 to 30 August 2017. Red (blue) arrows are for surface velocity higher (lower) than 15 cm/s, the hypothetical threshold for which the westward ISOW deep flow is disrupted by deep-reaching velocities of the North Atlantic Current. Bathymetry (m) is colored in gray (the darkest shade indicates the shallowest areas). The gray line shows the 3,500-m isobath. The northern and the southern valleys of the Charlie-Gibbs Fracture Zone are identified with their initial letters (NV and SV). Yellow dots show the locations of profiles measured during each period; the black dots represents the starting point of float displacements. (right panels) Results of the Optimum Multiparameter analysis on the 37.03 σ_2 isopycnal averaged for the profiles displayed on the left panels (yellow dots). NEADW = North East Atlantic Deep Water; IW = Intermediate Water; LSW = Labrador Sea Water; ISOW = Iceland-Scotland Overflow Water.

3.4. Westward Advection of the Deep Flow From the CGFZ

This section discusses the fate of the deep vein that carries ISOW and NEADW westward in the CGFZ. We selected OMP results for which the deep floats obviously headed west in and beyond the northern and the southern valley of the CGFZ. Indeed, the comparison between the float trajectories and the surface currents (Figures 8–10) shows that in some cases the surface currents influenced the float trajectories either during their ascent and descent or because the NAC was sufficiently intense (that is when its eastward surface velocities exceeded 15 cm/ s) to disrupt or reverse the deep westward flow (Figure 10). For the northern valley, we considered the four deep floats that collected oxygen data and retained all the profiles made over their first cycles between their launch position and 37.5°N (Table 3; section 3.1; Figures 2b and 2c). Beyond 37.5°N, we selected the profiles measured by DP15-3 up to Newfoundland Basin (up to Cycle 19) except Cycle 13 when the float deviated southward (Figure 2). The similar direction between the surface velocities and the float trajectory suggests an influence of a NAC meander on the trajectory of DP15-3, which could have been

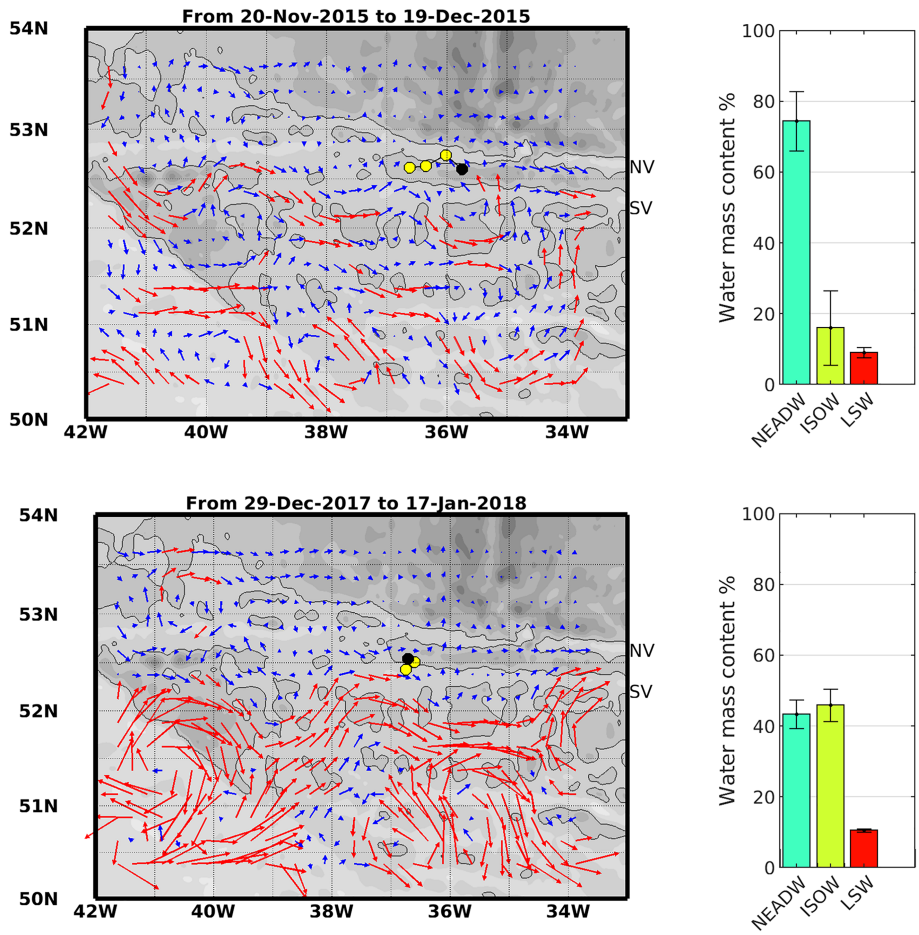

Figure 9. Same as Figure 8, but for the period between 20 November and 19 December 2015 (top panels) and the period between 29 December 2017 and 17 January 2018 (bottom panels).

temporarily deviated from the ISOW layer (Figure S7, top). For the southern valley and west of 38°W, we used all profiles with an evident westward displacement from DP17-2 (Table 3 and Figures 2a and 2c). Other cycles of DP17-2 acquired in the southern valley were not retained for this section because the surface velocities suggest an influence of the NAC on the float trajectory here as well (Figure S7, middle). It is important to note that all profiles selected in the CGFZ were positioned north of the NAC (see, e.g., Figures 8 and S8).

We considered the density range 37.01–37.05 σ_2, which encompasses the ISOW core level (37.03 σ_2; Figure 5) investigated in section 3.3. For conciseness, we (i) added the fraction of ISOW to that of NEADW, (ii) selected OMP results obtained for each density level between 37.01 σ_2 and 37.05 σ_2, and (iii) averaged the selected OMP results for six regions (R1 to R6; Figure 11) and estimated the uncertainties as the standard deviation of the OMP results in each of these regions. Profiles used for each of the six regions and θ, S, and O_2 errors are reported in Table 3. The fraction of ISOW explaining properties between 37.01 σ_2 and 37.05 σ_2 was nevertheless provided for the CGFZ area (R1–R3) to echo section 3.3.

In the northern and southern valleys of the CGFZ, the relative contribution of the ISOW-NEADW to the properties of the deep vein flowing westward was 89% (Figure 11). This relative contribution was dominated by ISOW, whose intensity was greater in the northern than in the southern valley.

The intensity of the relative contribution of the ISOW-NEADW signal decreased while spreading westward due to mixing with the shallower LSW and deeper DSOWi (Figure 11). At the exit of the CGFZ (R3, 40°W),

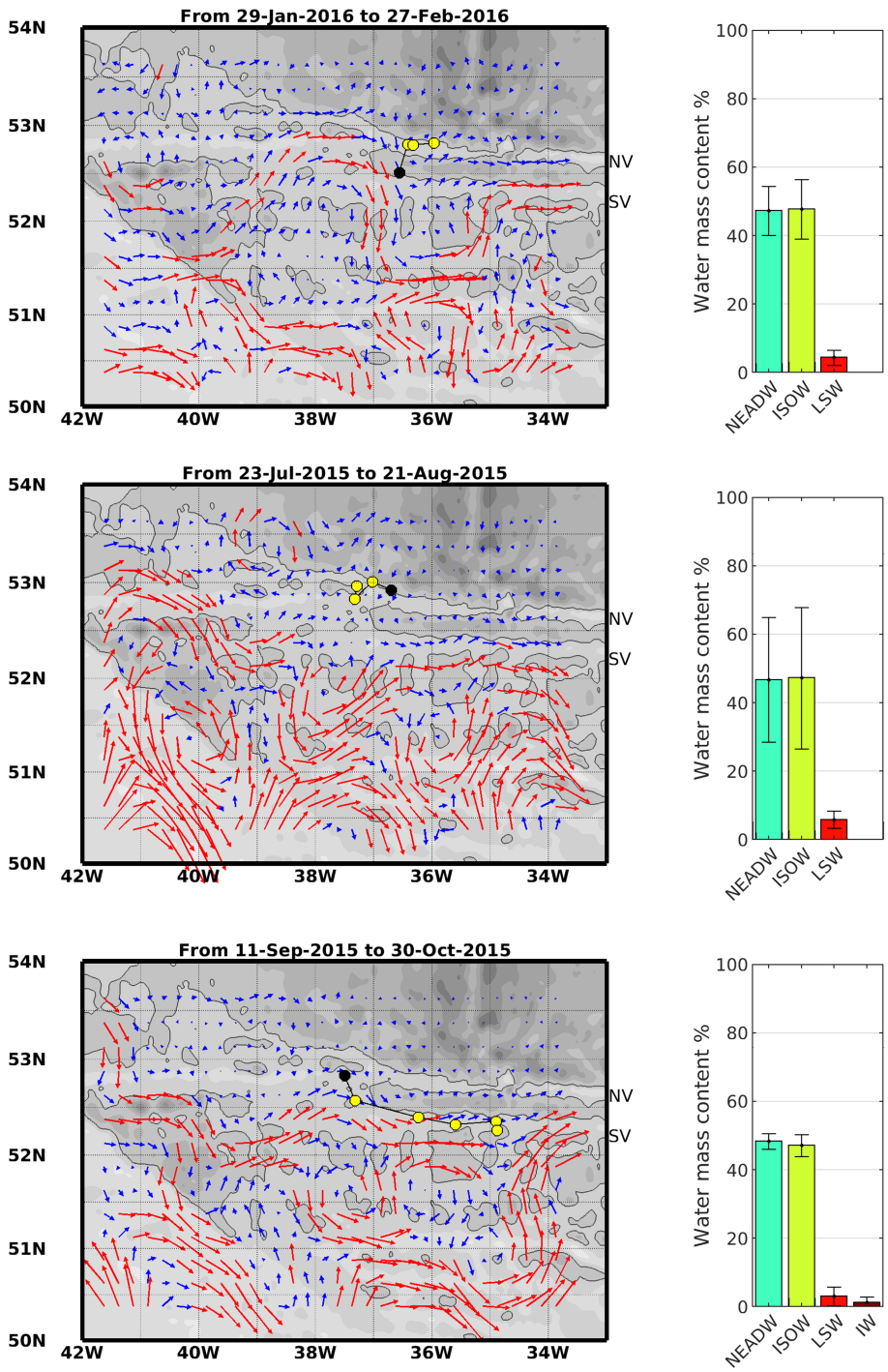

Figure 10. Same as Figure 8 but for the period between 29 January to 27 February 2016 (top panels), the period between 23 July and 21 August 2015 (middle panels), and the period between 11 September and 30 October 2015 (bottom panels).

properties in the ISOW layer were explained by those of ISOW-NEADW at 87 ± 5% in the northern valley and 70 ± 15% in the southern valley, which suggests that mixing with LSW and DSOWi was more intense in the southern valley. This could be explained by the proximity of the subpolar branch of the NAC that carries LSW eastward and by the recirculation of DSOW in the interior basin (Figure 9.15 in Talley et al., 2011). This westward dilution of the ISOW-NEADW signal is seen on the salinity sections from DP15-3 (Figure 5) and DP17-2 (Figure 4).

Table 3
RMS of the Residuals of the OMP Results Obtained Between 37.01 σ_2 and 37.05 σ_2 for Six Regions Along the Westward Path of the Deep-Argo Floats

Region	CGFZ	Float cycles	θ error (°C)	S error	O_2 error (μmol/kg)
R1 (35 to 36°W)	NV	DP15-3 Cycle 1 to 2; DP15-1 Cycle 1; DP15-2 Cycle 1; DP17-2 cy. 2 to 3	0.003	0.004	0.2
	SV	DP17-2 Cycle 13 to 14	0.005	0.002	0.5
R2 (36.5 to 38°W)	NV	DP15-3 Cycle 3 to 4; DP15-1 Cycle 2 to 3; DP15-2 Cycle 2 to 3	0.002	0.001	0.4
	SV	DP17-2 Cycles 15 and 18	0.006	0.002	1.7
R3 (38 to 40°W)	NV	DP15-3 Cycle 6 to 9	0.002	0.001	0.7
	SV	DP17-2 Cycles 22 and 29 to 31	0.003	0.002	0.9
R4 (40 to 43°W)		DP15-3 Cycles 10 to 12 and 14	0.004	0.003	0.8
R5 (43 to 46°W, >50°N)		DP15-3 Cycle 15 to 17	0.000	0.003	0.7
R6 (43 to 46°W, <50°N)		DP15-3 Cycle 19	0.001	0.008	1.4

Note. RMS = root-mean-square; OMP = Optimum Multiparameter; NV = northern valley; SV = southern valley.

Finally, OMP results along DP15-3 show that the relative contribution of ISOW-NEADW observed in the northern valley of the CGFZ is detectable up to the Newfoundland Basin. At 52°N to 46°W, properties of the deep vein were still mainly explained by ISOW-NEADW (65 ± 12%). The remainder was a mixture, with about the same proportions of DSOWi (18 ± 12%) and LSW (17 ± 4%). DP15-3 then reached the DWBC at R6 (near 49°N). There, properties of the deep vein resulted from mixing between DSOW (43 ± 7%), ISOW-NEADW (39 ± 4%), and LSW (18 ± 3%). Analysis of the surface dynamic conditions over Cycles 15–17 reveals large meanders and eddies in the area of the northwest corner of the NAC (44–46°W, 50–53°N; Figure 1), with surface velocities in the same direction as float displacements (Figure S7, bottom). These structures

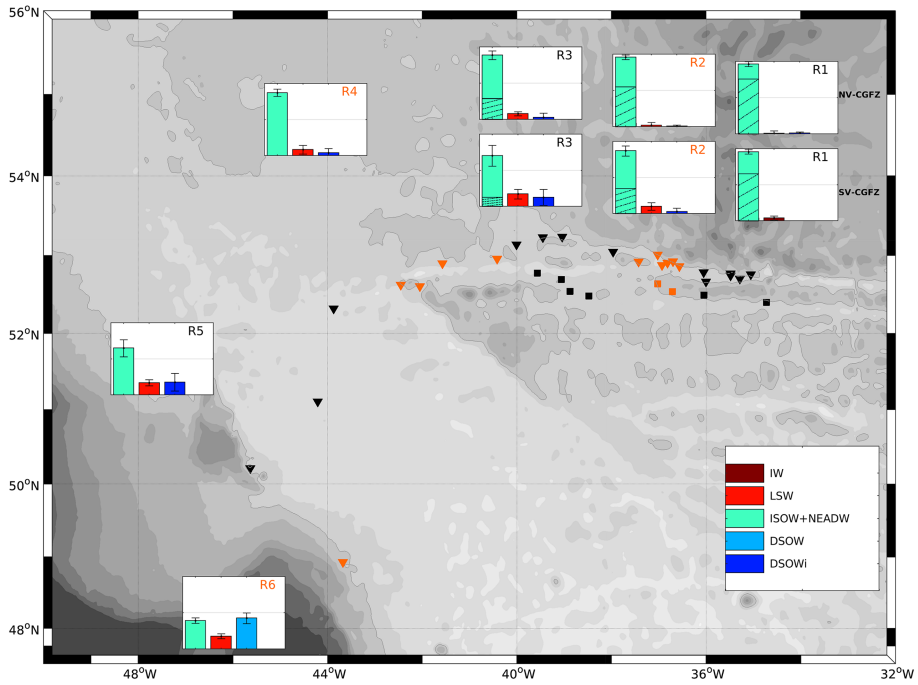

Figure 11. Westward evolution of the ISOW-NEADW signal from the CGFZ to the Deep Western Boundary Current. Bar plots with error bars show Optimum Multiparameter results averaged between 37.01 σ_2 and 37.05 σ_2 for six regions (R1 to R6) with their standard deviations. Dashed bar plots in the northern (NV) and southern (SV) valleys of the CGFZ representing the ISOW proportion of the deep vein. Corresponding profiles are given in Table 3 and indicated on the map with alternating colors to differentiate the regions: black for regions R1, R3, and R5 and orange for regions R2, R4, and R6. Profiles measured in the northern (southern) valley of the CGFZ are represented with a triangle (square). ISOW = Iceland-Scotland Overflow Water; DSOW = Denmark Strait Overflow Water; DSOWi = interior DSOW; DW = deep water; LSW = Labrador Sea Water; IW = Intermediate Water; NEADW = North East Atlantic Deep Water; CGFZ = Charlie-Gibbs Fracture Zone.

from the NAC probably contributed to the westward evolution of the ISOW-NEADW signal toward the DWBC. The high float displacement speed estimated over these periods (above 20 cm/ s) supports this hypothesis.

4. Discussion and Conclusion

During summers 2015 and 2017, five Deep-Argo floats were deployed in the northern valley of the CGFZ to drift at 2,750 dbar in the ISOW layer. As expected, the floats were first carried westward in the CGFZ by the westward flow of the ISOW layer in opposite direction to the upper current. Although they generally moved westward during their stay in the CGFZ, the float displacement was perturbed between 36°W and 38°W where some floats moved northward, southward or recirculated eastward. The two floats that recirculated eastward drifted either in the southern or northern valley. They went back westward after few cycles without going east of 34.5°W. Two floats eventually turned northward toward the Irminger basin in agreement with the known ISOW pathway but premature float death prevented further investigations. Finally, two floats (DP15-3 and DP17-2) made measurements beyond the CGFZ, and one of them reached the Newfoundland basin and drifted in the area dominated by the NAC.

The analysis of surface dynamic conditions derived from AVISO maps suggests that the pathway followed by a float in the CGFZ depends on whether or not northward intrusions of the eastward flowing NAC with deep-reaching velocities are present over the valleys of the CGFZ. One clear example is when a float drifted eastward in the southern valley of the CGFZ below the NAC (Figure 10, bottom). One can also note that two eddies coming from the NAC were present downstream of the initial westward trajectory of the deep floats: the first eddy was centered at 39°W to 53.5°N in July 2015 and the second at 37.5°W to 52.5°N in August 2017 (Figure 8, left). The presence of those eddies with potentially deep reaching velocities might explain changes in the direction of the float trajectories observed between 36° W and 38°W one month after their deployments (Figure 2 and section 3.1).

One float revealed a direct route for ISOW from the CGFZ toward the DWBC at Flemish Cap. The westward spreading of the deep vein between the CGFZ and Flemish cap was initially suggested from hydrographic sections (McCartney, 1992; Smethie & Fine, 2001; Stramma et al., 2004) but had never been sampled directly. It was also simulated by the eddy-resolving (1/12°) Atlantic simulations from Xu et al. (2010). Moreover, those authors pointed out that the westward pathway probably followed a route along the 3,500-m isobath, which is consistent with the float path seen in Figure 2. Beyond the CGFZ, this study showed that the westward flow of the ISOW layer from the CGFZ was advected by the NAC meandering close to the northwest corner to the DWBC north of Flemish Cap. This is in line with the southern increase in salinity observed along the Newfoundland coast by McCartney (1992), Smethie and Fine (2001), and Stramma et al. (2004). While the numerical model of Xu et al. (2010) showed that the westward route finally turned north between 46°W and 48°W to reach the DWBC south of the Cape Farewell, it highlighted a deep circulation dominated by eddies close to the northwest corner area in agreement with our observations. At Flemish Cap, our float was captured by the NAC and returned to the CGFZ with a chaotic trajectory (Figure 2). Finally, the differentiation between this westward route and the northward ISOW route toward the Irminger basin occurs west of 36°W in the numerical model of Xu et al. (2010). Although we have not been able to investigate this northward ISOW route in the present study, changes in the float trajectory that occur between 36°W and 38° W are consistent with the results of Xu et al. (2010).

Oxygen data acquired by the floats in the CGFZ revealed that the ISOW layer, characterized by salinity higher than 34.94 and density greater than 27.80 kg/ m^3 (Saunders, 1996), was mainly composed of the highly oxygenated ISOW and less oxygenated NEADW. Based on an OMP analysis, we showed varying relative contributions of the two water masses in the ISOW layer in the CGFZ. ISOW was generally dominant in the northern valley, but its contribution decreased when eddies or meanders of the NAC with deep-reaching velocities were present there. Although NEADW was detected in both valleys, its contribution compared with that of ISOW was larger in the southern valley than in the northern valley (Figures 8–11), probably because less ISOW goes that way. Only a volumetric analysis would allow a conclusion to be made on this. All of these results support the hypothesis that northward intrusions of the NAC into the CGFZ reduce the latitudinal extension of ISOW and favor its mixing with NEADW. Like ISOW, NEADW is defined by salinity higher than 34.94 below 27.80 σ_0 in the CGFZ (Table 2 and Figures 6 and 7), which means that

discrimination between the two water masses is possible with oxygen measurements (and with other biogeochemical tracers such as silicate measurements; van Aken, 2000). As oxygen was not measured by Bower and Furey (2017), they could not observe the signature of NEADW with their moorings in the CGFZ, in particular during strong interaction between the NAC and the deep westward flow.

OMP results showed that the ISOW-NEADW signal flowing westward from the CGFZ toward the DWBC was progressively diluted by LSW and DSOW. LSW and DSOW are two water masses carried from the western basin to the CGFZ by the subpolar branch of the NAC system. These results suggest that the mixing between ISOW, LSW, and DSOW in the western basin is a potential source of the NEADW. This complex water mass (NEADW-ISOW-LSW-DSOW) probably returns to the eastern basin within the NAC system, as suggested in the deep circulation scheme of Daniault et al. (2016). An oxygenated NEADW might suggest a westward origin whereas a low oxygenated NEADW would come from the eastern basin. More data, including O_2 measurements, from moorings, ships, or autonomous platforms would be necessary to refine the complex relationships between these four water masses and to better understand mechanisms involved in the interactions with the NAC.

Regular acquisition of oxygen measurement is now essential to better understand the oceanic response to global warming. O_2 is classically used to investigate key physical processes such as air-sea interactions (Maze et al., 2012), deep-convection (Piron et al., 2017) and ventilation, deep circulation, and water mass mixing (this study). O_2 measurements are also necessary to improve estimates of the oceanic uptake of anthropogenic CO_2, to monitor the impact of global warming on global oceanic oxygen content (Schmidtko et al., 2017) or to investigate decadal to seasonal changes in net community and export production (Gruber et al., 2010). There is thus a strong effort in the scientific community to set up and maintain a long term observing systems that will produce a homogeneous and validated O_2 data set.

Acknowledgments
The authors thank two anonymous reviewers for their fruitful and meaningful comments that helped improve this manuscript. They also thank their colleagues and ship crews of the N.O. Thalassa and the N.O. Atalante involved in the Deep-Argo float deployment and hydrographic acquisition of the RREX cruise data discussed in this paper. V. Racapé and V. Thierry were supported by the French Institute for the Exploitation of the Sea (IFREMER, Plouzané, France) and H. Mercier and C. Cabanes by the French National Centre for Scientific Research (CNRS). The Deep-Argo floats were funded by the EQUIPEX NAOS (Novel Argo Observing System) project funded by the French National Research Agency (ANR) under Reference ANR-10-EQPX-40. The work was supported by the French Oceanographic Fleet (TGIR FOF) for the realization of the RREX cruises and by the AtlantOS project funded by the European Union's Horizon 2020 research and innovation program under Agreement 633211. Deep-Argo data used in this study are available in the Argo database (Argo, 2000; at www.argodatamgt.org). The RREX data set is available at https://doi.org/10.17882/55445 (Thierry, Mercier, et al., 2018). The AVISO altimeter data were downloaded from the Copernicus Marine Environment Monitoring Service website (http://marine.copernicus.eu/services-portfolio/access-to-products/).

References

Argo (2000). Argo float data and metadata from Global Data Assembly Centre (Argo GDAC). SEANOE. https://doi.org/10.17882/42182

Beaird, N. L., Rhines, P. B., & Eriksen, C. C. (2013). Overflow waters at the Iceland–Faroe Ridge observed in multiyear seaglider surveys. *Journal of Physical Oceanography*, *43*(11), 2334–2351. https://doi.org/10.1175/JPO-D-13-029.1

Bittig, H. C., Fiedler, B., Fietzek, P., & Körtzinger, A. (2015). Pressure response of Aanderaa and Sea-Bird oxygen optodes. *Journal of Atmospheric and Oceanic Technology*, *32*(12), 2305–2317. https://doi.org/10.1175/JTECH-D-15-0108.1

Bower, A., & Furey, H. (2017). Iceland-Scotland Overflow Water transport variability through the C harlie-G ibbs F racture Z one and the impact of the North Atlantic Current. *Journal of Geophysical Research: Oceans*, *122*, 6989–7012. https://doi.org/10.1002/2017JC012698

Bower, A. S., & von Appen, W. J. (2008). Interannual variability in the pathways of the North Atlantic Current over the Mid-Atlantic Ridge and the impact of topography. *Journal of Physical Oceanography*, *38*(1), 104–120. https://doi.org/10.1175/2007JPO3686.1

Branellec, P. & Thierry, V. (2016). RREX 2015, CTD-O2 data report. ODE/ LOPS/16-26. https://doi.org/10.13155/47156

Branellec, P. & Thierry, V. (2018). RREX 2017, CTD-O2 data report. Rap. Int. LOPS/ 18-04. https://doi.org/10.13155/58074

Cabanes, C., Racapé, V. & Thierry, V. (2018), Delayed mode analysis of Deep Avor Float. SO. ARGO – LOPS report n°LOPS/ 18-03. http://archimer.ifremer.fr/doc/00443/55464/

Cabanes, C., Thierry, V., & Lagadec, C. (2016). Improvement of bias detection in Argo float conductivity sensors and its application in the North Atlantic. *Deep Sea Research Part I: Oceanographic Research Papers*, *114*, 128–136. https://doi.org/10.1016/j.dsr.2016.05.007

Daniault, N., Mercier, H., Lherminier, P., Sarafanov, A., Falina, A., Zunino, P., et al. (2016). The northern North Atlantic Ocean mean circulation in the early 21st century. *Progress in Oceanography*, *146*, 142–158. https://doi.org/10.1016/j.pocean.2016.06.007

de Jong, M. F., & de Steur, L. (2016). Strong winter cooling over the Irminger Sea in winter 2014–2015, exceptional deep convection, and the emergence of anomalously low SST. *Geophysical Research Letters*, *43*, 7106–7113. https://doi.org/10.1002/2016GL069596

Dickson, R., Lazier, J., Meincke, J., Rhines, P., & Swift, J. (1996). Long-term coordinated changes in the convective activity of the North Atlantic. *Progress in Oceanography*, *38*(3), 241–295. https://doi.org/10.1016/S0079-6611(97)00002-5

Dickson, R. R., & Brown, J. (1994). The production of North Atlantic Deep Water: Sources, rates, and pathways. *Journal of Geophysical Research*, *99*(C6), 12319–12341. https://doi.org/10.1029/94JC00530

Falina, A., Sarafanov, A., Mercier, H., Lherminier, P., Sokov, A., & Daniault, N. (2012). On the cascading of dense shelf waters in the Irminger Sea. *Journal of Physical Oceanography*, *42*(12), 2254–2267. https://doi.org/10.1175/JPO-D-12-012.1

Falina, A., Sarafanov, A., & Sokov, A. (2007). Variability and renewal of Labrador Sea Water in the Irminger Basin in 1991–2004. *Journal of Geophysical Research*, *112*(C1), C01006. https://doi.org/10.1029/2005jc003348

Fleischmann, U., Hildebrandt, H., Putzka, A., & Bayer, R. (2001). Transport of newly ventilated deep water from the Iceland Basin to the West European Basin. *Deep Sea Research Part I: Oceanographic Research Papers*, *48*(8), 1793–1819. https://doi.org/10.1016/S0967-0637(00)00107-2

Gallian, M., & Thierry, V. (2018). Delayed-mode quality control of dissolved oxygen concentration measured by ARGO floats in the North-Atlantic with LOCODOX - Floats deployed in 2012, 2014, 2015, 2016 and 2017. https://doi.org/10.13155/58314

Garcia, H. E., Locarnini, R. A., Boyer, T. P., Antonov, J. I., Baranova, O. K., Zweng, M. M., & Johnson, D. R. (2010). In S. Levitus (Ed.), *World Ocean Atlas 2009, Volume 3: Dissolved Oxygen, Apparent Oxygen Utilization, and Oxygen Saturation*, *NOAA Atlas NESDIS* (Vol. 70). Washington, D.C: U.S. Government Printing Office.

Garcia-Ibanez, M. I., Pardo, P. C., Carracedo, L. I., Mercier, H., Lherminier, P., Rios, A. F., & Perez, F. F. (2015). Structure, transports and transformations of the water masses in the Atlantic Subpolar Gyre. *Progress in Oceanography*, *135*, 18–36. https://doi.org/10.1016/j.pocean.2015.03.009

Gruber, N., Doney, S. C., Emerson, S. R., Gilbert, D., Kobayashi, T., Kortzinger, A., et al. (2010). Developing a Global In Situ Observatory for Ocean Deoxygenation and Biogeochemistry. In J. Hall, D. E. Harrison, & D. Stammer (Eds.), *Proceedings of OceanObs'09: Sustained Ocean Observations and Information for Society* (Vol. *2*). Venice, Italy: ESA Publication WPP-306. https://doi.org/10.5270/OceanObs09.cwp.39

Hansen, B., & Østerhus, S. (2007). Faroe bank channel overflow 1995–2005. *Progress in Oceanography*, *75*(4), 817–856. https://doi.org/10.1016/j.pocean.2007.09.004

Harvey, J. & Arhan, M. (1988) The water masses of the central North Atlantic in 1983-84. *Journal of Physical Oceanography*, *18*, 1855–1875.

Johnson, G. C., Lyman, J. M., & Purkey, S. G. (2015). Informing deep Argo array design using Argo and full-depth hydrographic section data. *Journal of Atmospheric and Oceanic Technology*, *32*(11), 2187–2198. https://doi.org/10.1175/JTECH-D-15-0139.1

Kanzow, T., & Zenk, W. (2014). Structure and transport of the Iceland Scotland Overflow plume along the Reykjanes Ridge in the Iceland Basin. *Deep Sea Research Part I: Oceanographic Research Papers*, *86*, 82–93. https://doi.org/10.1016/j.dsr.2013.11.003

Kieke, D., & Rhein, M. (2006). Variability of the overflow water transport in the western subpolar North Atlantic, 1950–97. *Journal of Physical Oceanography*, *36*(3), 435–456. https://doi.org/10.1175/JPO2847.1

Kobayashi, T. (2019). Fresh salinity bias with negative pressure dependency found at SBE 41CP on Deep NINJA. Presentation (AST-20_201903_DeepNINJA_SensorBias_dual.pdf) at the 20th Argo Steering Team meeting in Hangzhou (China), March 2019. Available at. http://www.argo.ucsd.edu/AcAST-20_agenda.html

Lankhorst, M., & Zenk, W. (2006). Lagrangian observations of the middepth and deep velocity fields of the northeastern Atlantic Ocean. *Journal of Physical Oceanography*, *36*(1), 43–63. https://doi.org/10.1175/JPO2869.1

Lazier, J. R. N. (1973). The renewal of Labrador Sea water. *Deep Sea Research and Oceanographic Abstracts*, *20*(4), 341–353. https://doi.org/10.1016/0011-7471(73)90058-2

Le Reste, S., Dutreuil, V., André, X., Thierry, V., Renaut, C., Le Traon, P. Y., & Maze, G. (2016). "Deep-Arvor": A new profiling float to extend the Argo observations down to 4000-m depth. *Journal of Atmospheric and Oceanic Technology*, *33*(5), 1039–1055. https://doi.org/10.1175/JTECH-D-15-0214.1

Lozier, M. S., Li, F., Bacon, S., Bahr, F., Bower, A. S., Cunningham, S. A., et al. (2019). A sea change in our view of overturning in the subpolar North Atlantic. *Science*, *363*(6426), 516–521. https://doi.org/10.1126/science.aau6592

Mantyla, A. W. (1994). The treatment of inconsistencies in Atlantic deep water salinity data. *Deep Sea Research Part I: Oceanographic Research Papers*, *41*(9), 1387–1405. https://doi.org/10.1016/0967-0637(94)90104-X

Maze, G., Mercier, H., Thierry, V., Memery, L., Morin, P., & Perez, F. F. (2012). Mass, nutrient and oxygen budgets for the northeastern Atlantic Ocean. *Biogeosciences*, *9*(10), 4099–4113. https://doi.org/10.5194/bg-9-4099-2012

McCartney, M. S. (1992). Recirculating components to the deep boundary current of the northern North Atlantic. *Progress in Oceanography*, *29*(4), 283–383. https://doi.org/10.1016/0079-6611(92)90006-L

McCartney, M. S., & Talley, L. D. (1982). The subpolar mode water of the North Atlantic Ocean. *Journal of Physical Oceanography*, *12*(11), 1169–1188. https://doi.org/10.1175/1520-0485(1982)012<1169:TSMWOT>2.0.CO;2

McCartney, M. S., & Talley, L. D. (1984). Warm-to-cold water conversion in the northern North Atlantic Ocean. *Journal of Physical Oceanography*, *14*(5), 922–935. https://doi.org/10.1175/1520-0485(1984)014<0922:WTCWCI>2.0.CO;2

Mertens, C., Rhein, M., Walter, M., Böning, C. W., Behrens, E., Kieke, D., et al. (2014). Circulation and transports in the Newfoundland Basin, western subpolar North Atlantic. *Journal of Geophysical Research: Oceans*, *119*, 7772–7793. https://doi.org/10.1002/2014JC010019

Owens, W. B., & Wong, A. P. (2009). An improved calibration method for the drift of the conductivity sensor on autonomous CTD profiling floats by θ–S climatology. *Deep Sea Research Part I*, *56*(3), 450–457. https://doi.org/10.1016/j.dsr.2008.09.008

Petit, T., Mercier, H., & Thierry, V. (2018). First estimate of the volume and water mass transports across the Reykjanes Ridge. *Journal of Geophysical Research: Oceans*, *123*, 6703–6719. https://doi.org/10.1029/2018JC013999

Piron, A., Thierry, V., Mercier, H., & Caniaux, G. (2017). Argo float observations of basin-scale deep convection in the Irminger Sea during winter 2011–2012. *Deep Sea Research Part I: Oceanographic Research Papers*, *109*, 76–90. https://doi.org/10.1016/j.dsr.2015.12.012

Purkey, S. G., & Johnson, G. C. (2013). Antarctic Bottom Water Warming and Freshening: Contributions to Sea Level Rise, Ocean Freshwater Budgets, and Global Heat Gain. *Journal of Climate*. *26*:6105–6122. https://doi.org/10.1175/JCLI-D-12-00834.1

Saunders, P. M. (1994). The flux of overflow water through the Charlie-Gibbs Fracture Zone. *Journal of Geophysical Research*, *99*(C6), 12343–12355. https://doi.org/10.1029/94JC00527

Saunders, P. M. (1986) The accuracy of measurement of salinity, oxygen and temperature in the deep ocean. *Journal of Physical Oceanography*, *16*, 189-195

Saunders, P. M. (1996). The flux of dense cold overflow water southeast of Iceland. *Journal of Physical Oceanography*, *26*(1), 85–95. https://doi.org/10.1175/1520-0485(1996)026<0085:TFODCO>2.0.CO;2

Saunders, P. M. (2001). The dense northern overflows. In G. Siedler, J. Church, & J. Gould (Eds.), *Ocean Circulation and Climate* (Vol. 77, pp. 401–417). San Diego: Academic Press. https://doi.org/10.1016/S0074-6142(01)80131-5

Schmidtko, S., Stramma, L., & Visbeck, M. (2017). Decline in global oceanic oxygen content during the past five decades. *Nature*, *542*(7641), 335–339. https://doi.org/10.1038/nature21399

Schott, F., Stramma, L., & Fischer, J. (1999). Interaction of the North Atlantic current with the deep Charlie Gibbs Fracture Zone throughflow. *Geophysical Research Letters*, *26*(3), 369–372. https://doi.org/10.1029/1998GL900223

Smeed, D. A., McCarthy, G. D., Cunningham, S. A., Frajka-Williams, E., Rayner, D., Johns, W. E., Meinen, C. S., Baringer, M. O., Moat, B. I., Duchez, A., &Bryden, H. L. (2014). Observed decline of the Atlantic meridional overturning circulation 2004–2012. *Ocean Science*, *10*(1), 29–38. https://doi.org/10.5194/os-10-29-2014

Smethie, W. M. Jr., & Fine, R. A. (2001). Rates of North Atlantic Deep Water formation calculated from chlorofluorocarbon inventories. *Deep Sea Research Part I: Oceanographic Research Papers*, *48*(1), 189–215. https://doi.org/10.1016/S0967-0637(00)00048-0

Stramma, L., Kieke, D., Rhein, M., Schott, F., Yashayaev, I., & Koltermann, K. P. (2004). Deep water changes at the western boundary of the subpolar North Atlantic during 1996 to 2001. *Deep Sea Research Part I: Oceanographic Research Papers*, *51*(8), 1033–1056. https://doi.org/10.1016/j.dsr.2004.04.001

Sy, A., Rhein, M., Lazier, J. R. N., Koltermann, K. P., Meincke, J., Putzka, A., & Bersch, M. (1997). Surprisingly rapid spreading of newly formed intermediate waters across the north Atlantic Ocean. *Nature*, *386*, 675–679.

Takeshita, Y., Martz, T. R., Johnson, K. S., Plant, J. N., Gilbert, D., Riser, S. C., et al. (2013). A climatology-based quality control procedure for profiling float oxygen data. *Journal of Geophysical Research: Oceans*, *118*, 5640–5650. https://doi.org/10.1002/jgrc.20399

Talley, L. D., & McCartney, M. S. (1982). Distribution and circulation of Labrador Sea water. *Journal of Physical Oceanography*, *12*(11), 1189–1205. https://doi.org/10.1175/1520-0485(1982)012<1189:DACOLS>2.0.CO;2

Talley, L. D., Pickard, E., Emery, W. J., & Swift, J. H. (2011). *Descriptive physical oceanography: An introduction*, (Sixth ed.p. 560). Burlingham, MA: Elsevier. https://doi.org/10.1016/B978-0-7506-4552-2.10001-0

Tanhua, T., Olsson, K. A., & Jeansson, E. (2005). Formation of Denmark Strait overflow water and its hydro-chemical composition. *Journal of Marine Systems*, *57*(3-4), 264–288. https://doi.org/10.1016/j.jmarsys.2005.05.003

Thierry, V., Bittig, H. Gilbert, D., Kobayashi, T., Sato, K. & Schmid, C. (2018). Processing Argo OXYGEN data at the DAC level, v2.3.1, https://doi.org/10.13155/39795

Thierry, V., Mercier H., Petit T., Branellec P., Balem K., Lherminier P. (2018). Reykjanes Ridge Experiment (RREX) dataset. SEANOE. https://doi.org/10.17882/55445

Tomczak, M. Jr. (1981). A multi-parameter extension of temperature/ salinity diagram techniques for the analysis of non-isopycnal mixing. *Progress in Oceanography*, *10*(3), 147–171. https://doi.org/10.1016/0079-6611(81)90010-0

Tomczak, M., & Large, D. G. (1989). Optimum multiparameter analysis of mixing in the thermocline of the eastern Indian Ocean. *Journal of Geophysical Research*, *94*(C11), 16141–16149. https://doi.org/10.1029/JC094iC11p16141

Våge, K., Pickart, R. S., Sarafanov, A., Knutsen, Y., Mercier, H., Lherminier, P., et al. (2011). The irminger gyre: Circulation, convection, and interannual variability. *Deep Sea Research Part I: Oceanographic Research Papers*, *58*(5), 590–614. https://doi.org/10.1016/j.dsr.2011.03.001

van Aken, H. M. (2000). The hydrography of the mid-latitude northeast Atlantic Ocean: I: The deep water masses. *Deep Sea Research Part I: Oceanographic Research Papers*, *47*(5), 757–788. https://doi.org/10.1016/S0967-0637(99)00092-8

van Aken, H. M., & Becker, G. (1996). Hydrography and through-flow in the north-eastern North Atlantic Ocean: the NANSEN project. *Progress in Oceanography*, *38*(4), 297–346. https://doi.org/10.1016/S0079-6611(97)00005-0

van Aken, H. M., & de Boer, C. J. (1995). On the synoptic hydrography of intermediate and deep water masses in the Iceland Basin. *Deep Sea Research Part I: Oceanographic Research Papers*, *42*(2), 165–189. https://doi.org/10.1016/0967-0637(94)00042-Q

Worthington, L. V., & Volkmann, G. H. (1965). The volume transport of the Norwegian Sea overflow water in the North Atlantic. *Deep Sea Research and Oceanographic Abstracts*, *12*(5), 667–676. https://doi.org/10.1016/0011-7471(65)91865-6

Xu, X., Bower, A., Furey, H., & Chassignet, E. (2018). Variability of the Iceland-Scotland overflow water transport through the Charlie-Gibbs Fracture Zone: Results from an eddying simulation and observations. *Journal of Geophysical Research: Oceans*, *123*, 5808–5823. https://doi.org/10.1029/2018JC013895

Xu, X., Schmitz, W. J., Hurlburt, H. E., Hogan, P. J., & Chassignet, E. P. (2010). Transport of Nordic Seas overflow water into and within the Irminger Sea: An eddy-resolving simulation and observations. *Journal of Geophysical Research*, *115*, C12048. https://doi.org/10.1029/2010JC006351

Yashayaev, I. (2007). Hydrographic changes in the Labrador Sea, 1960–2005. *Progress in Oceanography*, *73*(3-4), 242–276. https://doi.org/10.1016/j.pocean.2007.04.015

Yashayaev, I., & Loder, J. W. (2016). Recurrent replenishment of Labrador Sea Water and associated decadal-scale variability. *Journal of Geophysical Research: Oceans*, *121*, 8095–8114. https://doi.org/10.1002/2016JC012046

Zou, S., Lozier, S., Zenk, W., Bower, A., & Johns, W. (2017). Observed and modeled pathways of the Iceland Scotland Overflow Water in the eastern North Atlantic. *Progress in Oceanography*, *159*, 211–222. https://doi.org/10.1016/j.pocean.2017.10.003